Journal of Power Sources 679 (2026) 240179

Contents lists available at ScienceDirect

Journal of Power Sources

journal homepage: www.elsevier.com/locate/jpowsour

Sublimation-assisted formation of hollow N-doped graphitic carbon/reduced graphene oxide frameworks hosting biphasic iron selenide nanocrystals for high performance sodium-ion storage

Jae Seob Lee [a,b,1], Ji Hun Baek [a,1], Rakesh Saroha [a,c], Jae-Oh Shim [d], Chungyeon Cho [e], Sang Mun Jeong [f], Gi Dae Park [g,*], Yun Chan Kang [b,**], Jung Sang Cho [a,h,i,***]

[a] Department of Engineering Chemistry, Chungbuk National University, Chungbuk, 28644, Republic of Korea
[b] Department of Materials Science and Engineering, Korea University, Anam-Dong, Seoul, Seongbuk-Gu, 02841, Republic of Korea
[c] Department of Materials Science and Engineering, Ajou University, 206 Worldcup-ro, Yeongtong-gu, Suwon-si, Gyeonggi-do, 16499, Republic of Korea
[d] Department of Chemical Engineering/Nanoscale Environmental Sciences and Technology Institute, Wonkwang University, Iksan, Jeonbuk, 54538, Republic of Korea
[e] Department of Biomedical Materials Science, Jeonbuk Advanced Bio-convergence Academy, Wonkwang University, Iksan, Jeonbuk, 54538, Republic of Korea
[f] Department of Chemical Engineering, Chungbuk National University, Chungbuk, 28644, Republic of Korea
[g] Department of Advanced Materials Engineering, Chungbuk National University, Chungbuk, 28644, Republic of Korea
[h] Biomedical Research Institute, Chungbuk National University Hospital, Chungbuk, 28644, Republic of Korea
[i] Advanced Energy Research Institute, Chungbuk National University, Cheongju, Chungbuk, 28644, Republic of Korea

HIGHLIGHTS

- Fe_xSe_y@NGC/rGO hollow nanofibers were synthesized by electrospinning.
- Uniform $FeSe_2/Fe_3Se_4$ domains provide synergistic and rapid redox kinetics.
- RGO and N-doped graphitic carbon (NGC) enhance conductivity and buffer volume change.
- Longitudinal hollow channels enable fast Na-ion diffusion and electrolyte access.
- The hierarchical design ensures stable cycling even at high current densities.

GRAPHICAL ABSTRACT

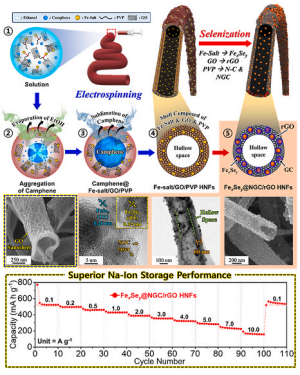

ARTICLE INFO

Keywords:
Sodium-ion battery
Electrospinning
Hollow nanofiber

ABSTRACT

Achieving fast reaction kinetics and robust structural stability under repeated sodiation/de-sodiation cycling is essential for high-rate and long-life sodium-ion batteries (SIBs). In this work, a sublimation-driven architecture engineering strategy is introduced to construct hollow N-doped graphitic carbon/reduced graphene oxide (NGC/rGO) frameworks hosting uniformly dispersed biphasic iron selenide nanocrystals ($FeSe_2/Fe_3Se_4$), denoted as

* Corresponding author.Department of Advanced Materials Engineering, Chungbuk National University, Chungbuk 28644, Republic of Korea.
** Corresponding author.Department of Materials Science and Engineering, Korea University, Anam-Dong, Seongbuk-Gu, Seoul 02841, Republic of Korea.
*** Corresponding author. Department of Engineering Chemistry, Chungbuk National University, Chungbuk 28644, Republic of Korea.
E-mail addresses: gdpark@chungbuk.ac.kr (G.D. Park), yckang@korea.ac.kr (Y.C. Kang), jscho@cbnu.ac.kr (J.S. Cho).
[1] These authors contributed equally to this work.

https://doi.org/10.1016/j.jpowsour.2026.240179
Received 27 January 2026; Received in revised form 7 April 2026; Accepted 19 April 2026
Available online 23 April 2026

Reduced graphene oxide
Biphasic iron selenide

Fe_xSe_y@NGC/rGO HNFs. This hierarchical structure integrates three synergistic design elements: (i) camphene-templated hollow tunnels that provide uninterrupted ion-diffusion channels and exceptional stress-buffering capability, (ii) a conductive NGC/rGO dual-carbon network that ensures rapid electron transport and stabilizes the interphase during deep sodiation, and (iii) a complementary $FeSe_2$/Fe_3Se_4 biphasic composition that enables phase-dependent reaction pathways, enhancing reversibility and accelerating conversion kinetics. Benefiting from this multi-level structural and compositional synergy, the Fe_xSe_y@NGC/rGO HNF anode delivers outstanding rate capability up to 10.0 A g^{-1} and remarkable long-term cycling stability at 0.5–2.0 A g^{-1}, outperforming most iron selenide-based anodes reported to date. This work demonstrates a generalizable materials-design paradigm that combines sublimation-induced hollow carbon frameworks with phase-engineered chalcogenides to advance next-generation SIBs for large-scale energy storage.

1. Introduction

The rapidly growing demand for large-scale energy storage has accelerated the search for sustainable and economically viable technologies. While lithium-ion batteries (LIBs) have transformed portable electronics and electric vehicles, concerns over lithium scarcity, uneven geographical distribution, and increasing raw-material costs (~13,300 USD ton^{-1}) pose critical challenges to their long-term sustainability [1–3]. These limitations have shifted attention toward sodium-ion batteries (SIBs), which benefit from the natural abundance and wide availability of sodium, offering a pathway to reducing the levelized cost of storage for grid-oriented applications [4–6]. However, the larger ionic radius of Na-ion (1.02 Å) compared with Li-ion (0.76 Å) leads to sluggish diffusion kinetics, poor graphite intercalation, and severe structural deformation during repeated cycling, ultimately resulting in mechanical degradation and poor rate capability [7–11]. Such challenges necessitate the development of anode materials that combine rapid reaction kinetics with robust structural stability [12].

Transition-metal chalcogenides (TMCs) have emerged as promising candidates for SIB anodes due to their high theoretical capacities and favorable conversion mechanisms [13–17]. Among them, iron selenides (Fe_xSe_y) are particularly attractive because of their high theoretical capacities ($FeSe_2$: 500 mA h g^{-1}; Fe_3Se_4: 480 mA h g^{-1}) and intrinsically fast electrochemical reactions [18]. Nevertheless, TMCs typically undergo substantial volume changes during Na-ion conversion reactions, causing structural pulverization and rapid capacity decay [16]. Furthermore, their electrochemical behavior varies depending on phase composition: $FeSe_2$ exhibits semiconducting characteristics (E_g = 1.0 eV) but operates at a relatively high oxidation potential (~2.3 V *vs.* Na^+/Na), whereas Fe_3Se_4, with semi-metallic behavior (E_g = 0.5 eV), reacts at a lower potential (~1.5 V *vs* Na^+/Na), making it more suitable for anode operation [19,20]. These two phases also differ markedly in crystal structure; $FeSe_2$ has a compact orthorhombic marcasite-type lattice that restricts Na-ion transport, while Fe_3Se_4 possesses a vacancy-ordered pyrrhotite-like structure that provides more accessible interstitial sites and facilitates faster Na-ion diffusion [21,22]. Nevertheless, synthesizing phase-pure Fe_3Se_4 remains challenging, and its considerable volume expansion limits practical durability. Therefore, the controlled construction of biphasic iron selenides provides an appealing route to combine complementary properties—balancing electronic conductivity, reaction potential, and structural reversibility–toward high-performance SIB anodes.

To mitigate volume fluctuations during Na-ion cycling, numerous structural engineering strategies have been proposed for conversion-type anodes [23–25]. Among these approaches, hollow nanostructures have attracted significant attention due to their internal void space, which effectively buffers large volume changes and improves structural integrity under repeated cycling [26]. In parallel, one-dimensional (1D) architectures have been recognized as highly promising for electrochemical energy storage because of their shortened ion-diffusion paths, continuous electron-transport channels along the longitudinal axis, and excellent mechanical resilience [27]. Integrating hollow morphologies with 1D frameworks can therefore produce synergistic benefits—facilitating rapid Na-ion transport while maintaining structural resilience. Furthermore, because conversion-type materials generally suffer from intrinsically low electronic conductivity, the incorporation of conductive carbon frameworks is essential to enhance charge-transfer kinetics and ensure efficient electrochemical utilization [28,29]. Despite extensive studies on TMC-based anodes, the synergistic coupling of sublimation-created hollow carbon hosts with biphasic iron selenides has not yet been explored [25,30].

Guided by these considerations, a sublimation-induced process was employed to construct biphasic iron selenide nanocrystals encapsulated in N-doped graphitic carbon (NGC) and embedded within reduced graphene oxide (rGO) hollow nanofibers (Fe_xSe_y@NGC/rGO HNFs). In this architecture, the 1D hollow carbon framework provides internal buffering space and continuous ionic pathways, while the integrated NGC/rGO dual conductive network forms a highly efficient electron-transport matrix and simultaneously reinforces the mechanical stability of the composite. Moreover, the coexistence of $FeSe_2$ and Fe_3Se_4 phases offers complementary electrochemical characteristics; the semiconducting $FeSe_2$ contributes high theoretical capacity, whereas the semi-metallic Fe_3Se_4 enhances electronic conductivity and Na-ion diffusion. The integration of this biphasic composition with a mechanically robust hollow carbon host is expected to overcome the intrinsic limitations of conventional TMC anodes and enable high-performance sodium-ion storage.

2. Materials and methods

2.1. Sample preparation

Fe_xSe_y@NGC/rGO HNFs were synthesized via an electrospinning process followed by heat-treatment. Briefly, graphene oxide (GO) nanosheets were prepared from graphite flakes (Sigma-Aldrich, <20 μm, M_w = 12.01) *via* the modified Hummer's method [31]. The spinning solution was prepared by dispersing the prepared GO (0.25 g) in ethyl alcohol anhydrous (25 mL, SAMCHUN, 99.9%, M_w = 46.06) by ultrasonication for 1 h. Subsequently, 2.84 g of iron (III) acetylacetonate (Fe$(C_5H_7O_2)_3$, Acros Organics, 99%, M_w = 353.17), 4.0 g of camphene (Acros Organics, 75%, M_w = 136.24), and 1.5 g of polyvinylpyrrolidone (PVP, Alfa Aesar, M_w = ~1,300,000) were added, followed by overnight stirring to ensure complete homogenization. The prepared solution was loaded into a 12 mL plastic syringe fitted with a 23-gauge stainless steel needle at a flow rate of 2.0 mL h^{-1} onto a rotating drum collector (180 rpm) covered with aluminum foil. The distance and the applied voltage between the needle tip and drum collector were maintained at 20 cm and 20 kV. The as-spun Fe-salt/PVP/GO hollow nanofibers (HNFs) were stabilized at 150 °C for 3 days in a hot air oven. Finally, the stabilized HNFs were selenized using selenium powder (Se; SAMCHUN, 99.5%, M_w = 78.96) at 450 °C for 3 h under H_2/Ar atmosphere (vol = 4:96 %). For comparison, HNFs without rGO (abbreviated as Fe_xSe_y@NGC HNFs) and filled nanofibers (NFs) without camphene (referred to as Fe_xSe_y@NGC/rGO NFs) were also synthesized following the same procedure as discussed above.

2.2. Materials characterization

The structural and physicochemical properties of the synthesized nanofibers were comprehensively investigated using various characterization techniques. Crystal phase identification was performed *via* X-ray diffraction (XRD, Empyrean, Cu K_α radiation, $\lambda = 1.5418$ Å) at the Korea Basic Science Institute (Daedeok Main Center). Morphology and microstructure were examined using field-emission scanning electron microscopy (FE-SEM, S-4500, Hitachi) and field-emission transmission electron microscopy (FE-TEM, JEM-2100 F, JEOL). Additional TEM analyses were conducted using a JEM-120i microscope (JEOL) at the Department of Engineering Chemistry, Chungbuk National University. Thermogravimetric analysis (TGA, 209 F1 Libra, NETZSCH) was conducted in air atmosphere from 30 to 600 °C at a heating rate of 10 °C min^{-1} to assess the thermal and compositional stability. X-ray photoelectron spectroscopy (XPS, K-Alpha, Thermo Scientific, Al K_α source) was carried out at the Korea Basic Science Institute (Busan Center) to investigate the chemical bonding states and elemental composition. The elemental composition of prepared NFs were determined by inductively coupled plasma optical emission spectrometry (ICP-OES, Spectro ARCOS, SPECTRO Analytical Instruments). Specific surface area and pore size distribution were determined from nitrogen adsorption-desorption isotherms using Brunauer–Emmett–Teller (BET) and Barrett-Joyner-Halenda (BJH) methods. The carbon and nitrogen contents of the prepared NFs were quantified by elemental analysis (EA, vario MICRO cube, Elementar). Raman spectroscopy (RAMANtouch, Nanophoton) was employed to evaluate the crystallinity of the carbonaceous species.

2.3. Electrochemical measurements

Electrochemical properties of the prepared NFs was evaluated using 2032-type coin cells. Working electrodes were fabricated by blending active material, Super-P, and sodium carboxymethyl cellulose in a mass ratio of 7:2:1, followed by casting the resulting slurry onto copper foil. The coated electrode was dried overnight at 60 °C air oven, and subsequently punched into 14 mm diameter disks with an average mass loading of ~0.92 mg cm^{-2}. All cell assembly steps were conducted in an argon-filled glovebox to minimize exposure to moisture and oxygen. Metallic sodium and microporous polypropylene film (Celgard®2400, Wellcos) used as the counter/reference electrode and separator, respectively. The electrolyte consisted of 1.0 M $NaClO_4$ dissolved in a 1:1 (v/v) mixture of ethylene carbonate and dimethyl carbonate, with 5.0 wt% fluoroethylene carbonate as an additive. Galvanostatic discharge/charge cycling was performed over a voltage range of 0.01–3.0 V (*vs.* Na^+/Na) at various current densities (0.1–10 A g^{-1}) using a WBCS3000 battery cycler (WonATech). Cyclic voltammetry (CV) was carried out at a scan rate of 0.1 mV s^{-1}. Electrochemical impedance spectroscopy (EIS) was recorded in the frequency range of 100 kHz to 0.01 Hz with an AC amplitude of 10 mV.

3. Results and discussion

The formation mechanism of Fe_xSe_y@NGC/rGO HNFs is schematically illustrated in Scheme 1. During electrospinning, the precursor solution containing Fe-salt, PVP, GO, and camphene underwent spontaneous phase separation in ethanol due to polarity differences: the hydrophilic components (Fe-salt, PVP, and GO) formed the continuous matrix, while the hydrophobic camphene constituted the dispersed droplets (Scheme 1-①). Ethanol with its relatively high vapor pressure (~7.9 kPa at 25 °C) rapidly evaporated from the jet surface, whereas camphene with its substantially lower vapor pressure (~0.27 kPa at 25 °C) gradually migrated toward the fiber interior (Scheme 1-②). This difference in evaporation dynamics induced a radial viscosity gradient, driving inward camphene enrichment and droplet coalescence. Subsequent sublimation of camphene under ambient conditions produced a well-defined hollow interior within the as-spun HNFs (Scheme 1-③). Meanwhile, coordination interactions between the carbonyl groups of PVP and Fe^{3+} ions contributed to the stabilization of the outer shell, enabling the formation of continuous Fe-salt/PVP/GO HNFs (Scheme 1-

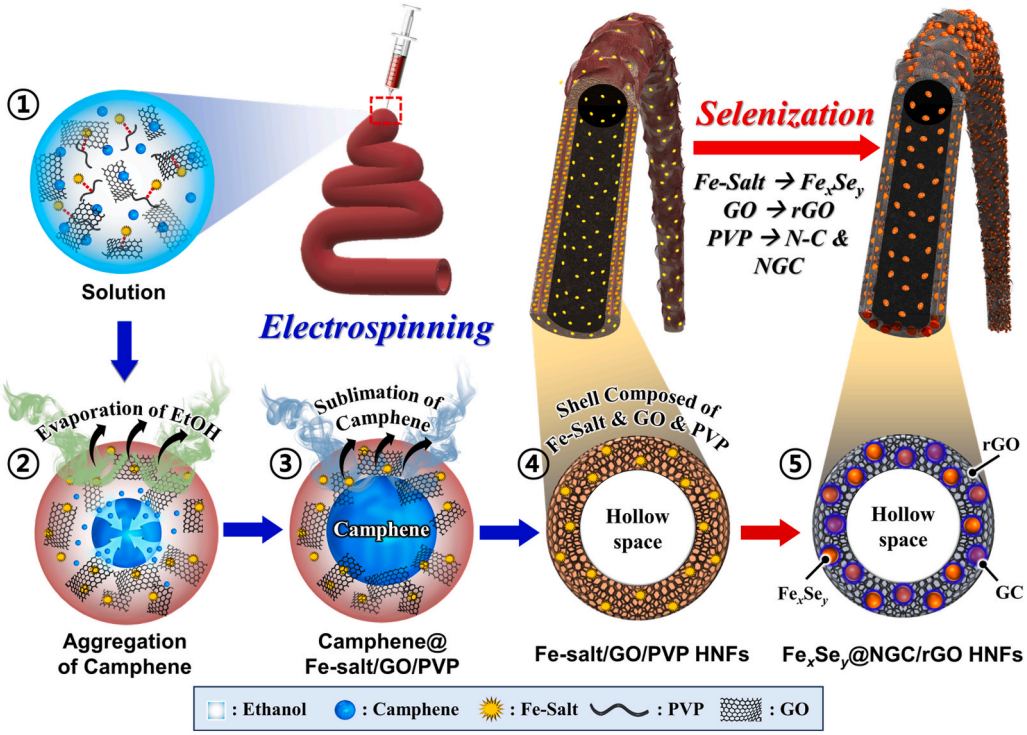

Scheme 1. Formation mechanism (①–⑤) of hollow N-doped graphitic carbon/reduced graphene oxide (NGC/rGO) frameworks hosting biphasic iron selenide nanocrystals (Fe_xSe_y) (Fe_xSe_y@NGC/rGO HNFs).

④). During the subsequent selenization step at 450 °C for 3 h under a 4% H_2/Ar atmosphere, the Fe-salt precursor was converted into uniformly distributed Fe_xSe_y nanocrystals within the carbonaceous matrix. The oxygen-containing functional groups of GO (such as hydroxyl and carboxyl groups) underwent thermal decomposition and removal, resulting in the formation of rGO with enhanced electrical conductivity. Simultaneously, PVP was carbonized into NGC, facilitated by the Fe-species acting as graphitization catalysts (Scheme 1-⑤). Through these sequential transformations, well-defined Fe_xSe_y@NGC/rGO HNFs were successfully obtained.

To gain deeper insights into the morphological and structural evolution during the synthesis process, detailed analyses were performed after each processing step. Fig. S1 presents the preliminary physical characterization of the as-spun Fe-salt/GO/PVP HNFs obtained after stabilization at 150 °C. The FE-SEM micrographs (Fig. S1a and b) reveal a continuous fibrous morphology without noticeable salt agglomeration, suggesting homogeneous precursor distribution. The cross-sectional image (Fig. S1b) clearly reveals the presence of camphene-derived longitudinal hollow channels, which are expected to facilitate electrolyte infiltration, shorten Na-ion diffusion pathways, and provide internal void space to buffer volume changes during electrochemical cycling. The XRD pattern (Fig. S1c) exhibits no sharp diffraction peaks, demonstrating the amorphous nature of the stabilized NFs. A broad hump centered at $2\theta = \sim 21^\circ$ corresponds to the GO framework embedded within the fibers. Raman spectroscopy (Fig. S1d) further elucidates the carbonaceous features, showing the characteristic D- and G-bands at 1365 and 1596 cm^{-1}, respectively, with a relative intensity ratio (I_D/I_G) of ~0.93 [32]. This ratio suggests the coexistence of disordered (sp^3) and graphitic (sp^2) carbon domains, which is beneficial for electrical conductivity and charge-transfer processes. To verify the incorporation and distribution of GO nanosheets, the stabilized HNFs were selectively oxidized at 350 °C for 1 h (Fig. S2) to remove PVP-derived amorphous carbon. After oxidation, distinct GO nanosheets were observed within the fibrous matrix (Fig. S2a and b), confirming their successful integration and highlighting their role in reinforcing the structural integrity and mechanical robustness of the composite framework.

The stabilized Fe-salt/GO/PVP HNFs were selenized at different temperatures (400, 450, and 500 °C) for 3 h under a H_2/Ar (4:96 vol%) atmosphere, and the resulting morphological, structural, and electrochemical characteristics are summarized in Fig. 1. FE-SEM images (Fig. 1a–c) show that all products retain the one-dimensional HNF architecture, while the secondary Fe_xSe_y nanoparticles decorating the HNF surface undergo substantial temperature-dependent evolution. At 400 °C (Fig. 1a), finely dispersed nanoparticles are uniformly distributed along the HNF surface. When the temperature is increased to 450 °C

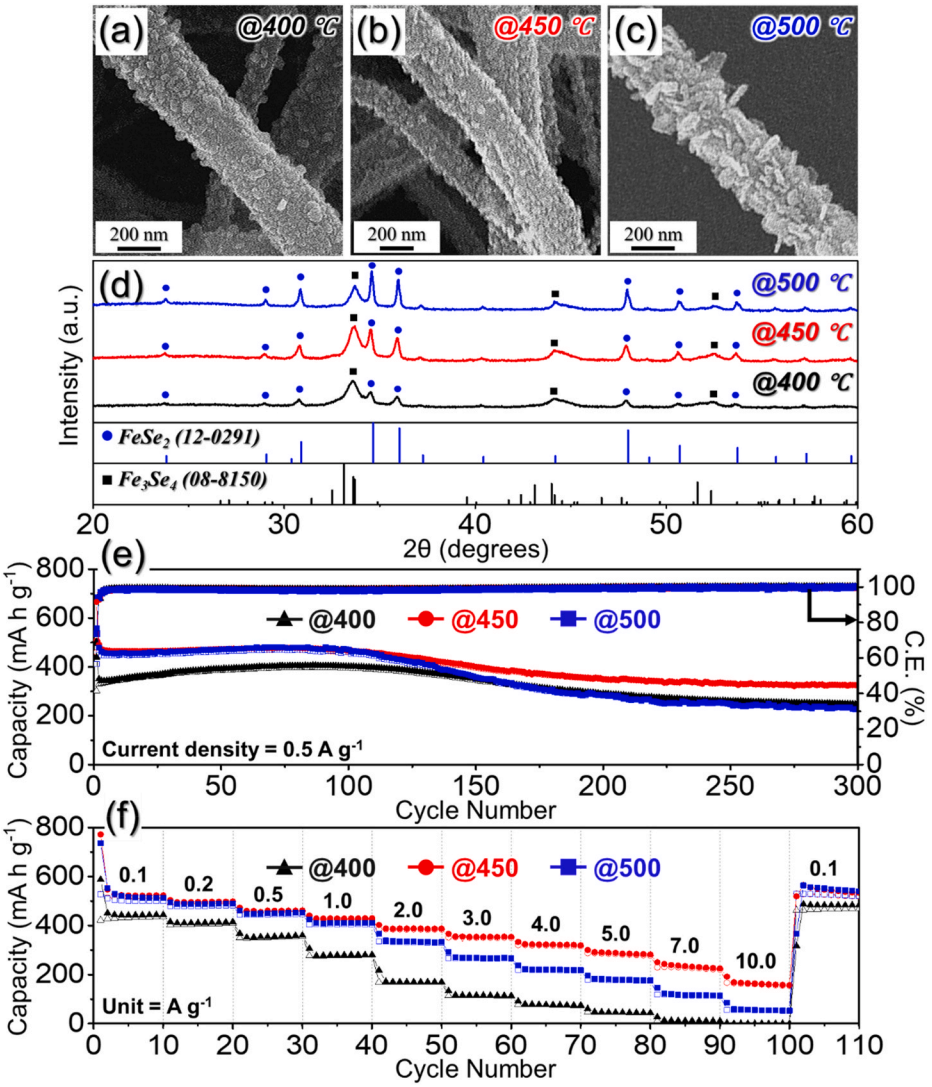

Fig. 1. (a–c) FE-SEM images, (d) XRD patterns, and (e, f) electrochemical properties of Fe_xSe_y@NGC/rGO HNFs after selenization at various temperatures under H_2/Ar atmosphere: (a) at 400 °C, (b) at 450 °C, (c) at 500 °C, (d) XRD patterns, (e) cycle performances at current density of 0.5 A g^{-1}, and (f) rate performances.

(Fig. 1b), the particles grow moderately and begin to form interconnected aggregates. Further increasing the temperature to 500 °C (Fig. 1c) leads to pronounced coarsening and the emergence of plate-like particles, indicating excessive grain growth at elevated temperature. The corresponding XRD patterns (Fig. 1d) reveal that all samples exhibit a biphasic structure composed of $FeSe_2$ and Fe_3Se_4 phases. Notably, as the selenization temperature increases from 400 to 500 °C, the relative intensity of the $FeSe_2$ reflections becomes progressively stronger, suggesting a higher fraction of this Se-rich phase at elevated temperatures. Although the same biphasic phases are present in all samples, their electrochemical behaviors differ markedly, indicating that Na-storage performance is influenced by the temperature-dependent evolution of the carbon framework and overall microstructure. At 400 °C, the carbon derived from PVP remains largely amorphous and the GO is only partially reduced, resulting in an underdeveloped NGC/rGO network with limited electronic connectivity [33]. Consequently, even though the Fe_xSe_y nanoparticles are fine and well dispersed, the electron transport pathways across the composite are insufficiently established. This limitation produces the largest voltage polarization ($\Delta V = 1.35$ V, Fig. S3), lowest initial discharge capacity at 0.5 A g^{-1} (Fig. 1e), and the poorest rate capability (Fig. 1f). When the selenization temperature is increased to 450 °C, both the carbon matrix and the embedded Fe_xSe_y nanoparticles evolve toward a more favorable state. Enhanced graphitization, more complete GO reduction, and consolidation of the HNF framework produce a continuous and conductive network that facilitates both electron transport and Na-ion diffusion. Raman spectra of the samples prepared at different temperatures (400, 450, and 500 °C) further support this structural evolution (Fig. S4a–c). All samples exhibit characteristic D- and G-bands corresponding to disordered and graphitic carbon structures. The I_D/I_G ratio decreases significantly from 0.92 at 400 °C to 0.84 at 450 °C, indicating an increased degree of graphitic ordering within the NGC/rGO framework and improved electrical conductivity. Interestingly, the I_D/I_G ratio for the 500 °C sample (0.83) is nearly identical to that of the 450 °C sample (0.84), suggesting that the degree of carbon graphitization reaches a plateau beyond 450 °C. EIS results of fresh electrodes further reveals the temperature-dependent kinetic behavior (Fig. S4d). The Nyquist plots show that the 450 °C sample exhibits the smallest charge-transfer resistance (R_{ct}), indicating the most efficient interfacial charge transport. The reduction in R_{ct} from 400 to 450 °C can be attributed to the combined effects of improved carbon conductivity and the favorable phase composition dominated by Fe_3Se_4. Notably, despite having a similar carbon quality to the 450 °C sample, the 500 °C sample shows an increased R_{ct}, which is reasonably attributed to the increased fraction of the $FeSe_2$ phase together with excessive particle coarsening at this temperature. Furthermore, the 450 °C sample displays the steepest slope in the Warburg region, indicating the fastest Na-ion diffusion kinetics. This behavior is consistent with the structural characteristics of Fe_3Se_4, which contains vacancy-ordered pathways that facilitate ion transport compared with the relatively compact marcasite-type lattice of $FeSe_2$. In contrast, the increased diffusion resistance at 500 °C can be attributed to the higher $FeSe_2$ fraction and the longer ion-transport pathways associated with particle coarsening. As a result, the 450 °C sample exhibits the smallest polarization ($\Delta V = 0.75$ V), the highest capacity at 0.5 A g^{-1} (Fig. 1e), and the best rate capability across all current densities (Fig. 1f). At 500 °C, excessive coarsening of Fe_xSe_y particles produces plate-like crystallites (Fig. 1c), which diminish the active surface area and lengthen Na-ion diffusion pathways. Additionally, partial densification or deformation of the carbon framework at this elevated temperature may hinder electrolyte penetration and diminish the structural benefits of the hollow interior. These effects lead to increased polarization ($\Delta V = 1.00$ V) and rapid performance degradation at high current densities (Fig. 1f), despite the larger $FeSe_2$ fraction. Collectively, these results indicate that the electrochemical trends—suboptimal behavior at 400 °C, optimal performance at 450 °C, and deterioration at 500 °C—are governed by the synergistic effects of carbon conductivity, phase composition, and microstructural stability rather than the $FeSe_2/Fe_3Se_4$ phase ratio alone. Therefore, 450 °C was identified as the optimal selenization temperature, providing the best balance among particle size, carbon conductivity, and structural robustness, and was thus selected for further in-depth characterization.

Following the identification of 450 °C as the optimal selenization temperature, the structural and chemical characteristics of the Fe_xSe_y@NGC/rGO HNFs were comprehensively investigated using FE-SEM, TEM/HR-TEM, XPS, and Raman spectroscopy (Fig. 2). FE-SEM images (Fig. 2a and b) confirm that the product retains a continuous 1D architecture with well-defined hollow interiors, while nanosized Fe_xSe_y particles are uniformly distributed along the nanofiber surface. TEM further verifies the hollow morphology, revealing a wall thickness of ~60 nm (Fig. 2c). HR-TEM imaging (Fig. 2d) shows distinct lattice fringes of 0.26 and 0.32 nm, corresponding to the (111) plane of $FeSe_2$ and the $(40\bar{1})$ plane of Fe_3Se_4, respectively, confirming the coexistence of both phases within the NFs. Notably, the Fe_xSe_y active materials are composed of ultrafine nanocrystals with sizes ranging from 5 to 20 nm (Fig. S5). A thin NGC layer encapsulates these biphasic nanocrystals, enabling intimate interfacial contact and efficient electron transfer to the surrounding rGO framework. The biphasic $FeSe_2/Fe_3Se_4$ nature is further validated by the SAED pattern (Fig. S6a). XPS analysis was conducted to probe the bonding configuration and chemical environments. The XPS survey spectrum (Fig. S6b) displays characteristic photoelectron signals corresponding to Fe 2*p*, O 1*s*, N 1*s*, C 1*s*, and Se 3*d*. The high-resolution Fe 2*p* spectrum (Fig. 2e) shows two main doublets at 710.6 and 724.3 eV (Fe $2p_{3/2}$ and Fe $2p_{1/2}$), along with satellite features ("*Sat.*"), consistent with previous reports [34–36]. Peak deconvolution reveals coexisting Fe^{2+} (710.4/724.1 eV) and Fe^{3+} (712.0/726.9 eV) species associated with Fe_3Se_4, while additional peaks at 706.8 and 719.6 eV confirm the presence of $FeSe_2$ [37,38]. The high-resolution Se 3*d* spectrum exhibits a broad envelope centered near 55.2 eV, resolvable into Fe–Se $3d_{3/2}$ (55.2 eV), Fe–Se $3d_{5/2}$ (54.3 eV), Fe 3*p* (53.1 eV), and Se–Se (56.0 eV) contributions, with a minor Se–O component appearing at 58.7 eV [39–44]. The C 1*s* spectrum (Fig. 2g) contains peaks corresponding to Fe–C, C=C, C–C/C–N, C=O, and O–C=O bonds [45–48]. A strong C=C signal indicates a high proportion of graphitized carbon species (rGO and NGC), while the Fe–C component suggests strong interfacial coupling between Fe_xSe_y nanocrystals and the carbon scaffold. The N 1*s* spectrum (Fig. 2h) is deconvoluted into four peaks at 398.3, 400.1, 401.8, and 403.7 eV, corresponding to the pyridinic-N, pyrrolic-N, graphitic-N, and oxidized N, respectively, confirming effective N-doping that enhances electronic conductivity and charge-transfer capability [48–51]. Elemental analysis (Table S1) further verifies an N content of 3.3 wt% in the carbon framework. TGA (Fig. S6c) shows four distinct mass-change regions: removal of adsorbed/crystal water below 200 °C, slight mass gain from oxidation of Fe_xSe_y to $FeSeO_x$, major mass loss between 300 and 500 °C due to SeO_2 sublimation and combustion of the NGC/rGO matrix, and a stable plateau above 500 °C corresponding to Fe_2O_3 formation. The carbon content estimated by EA results (Table S1) is approximately 31.6 wt%. Raman spectroscopy (Fig. 2i) shows characteristic D- and G-bands with an I_D/I_G ratio of 0.84, lower than that of the as-spun precursor (0.93; Fig. S1d), indicating enhanced graphitic ordering due to Fe-catalyzed carbon restructuring during selenization [32]. A weak and broadened second-order Raman feature in the 2400–3200 cm^{-1} region arising from overlapping D + D′ and 2D modes suggests the formation of partially graphitized yet defect-containing carbon frameworks, which is characteristic of heteroatom(N)-doped turbostratic carbon structures [52]. Additionally, a vibrational mode at 243.6 cm^{-1} confirms the presence of Fe–Se bonds [53]. Elemental mapping images (Fig. 2j) demonstrate homogeneous distribution of Fe, Se, C, and N throughout the NFs, confirming compositional uniformity.

To elucidate the structural roles of rGO and the hollow interior, two control samples—rGO-free Fe_xSe_y@NGC HNFs and filled Fe_xSe_y@NGC/

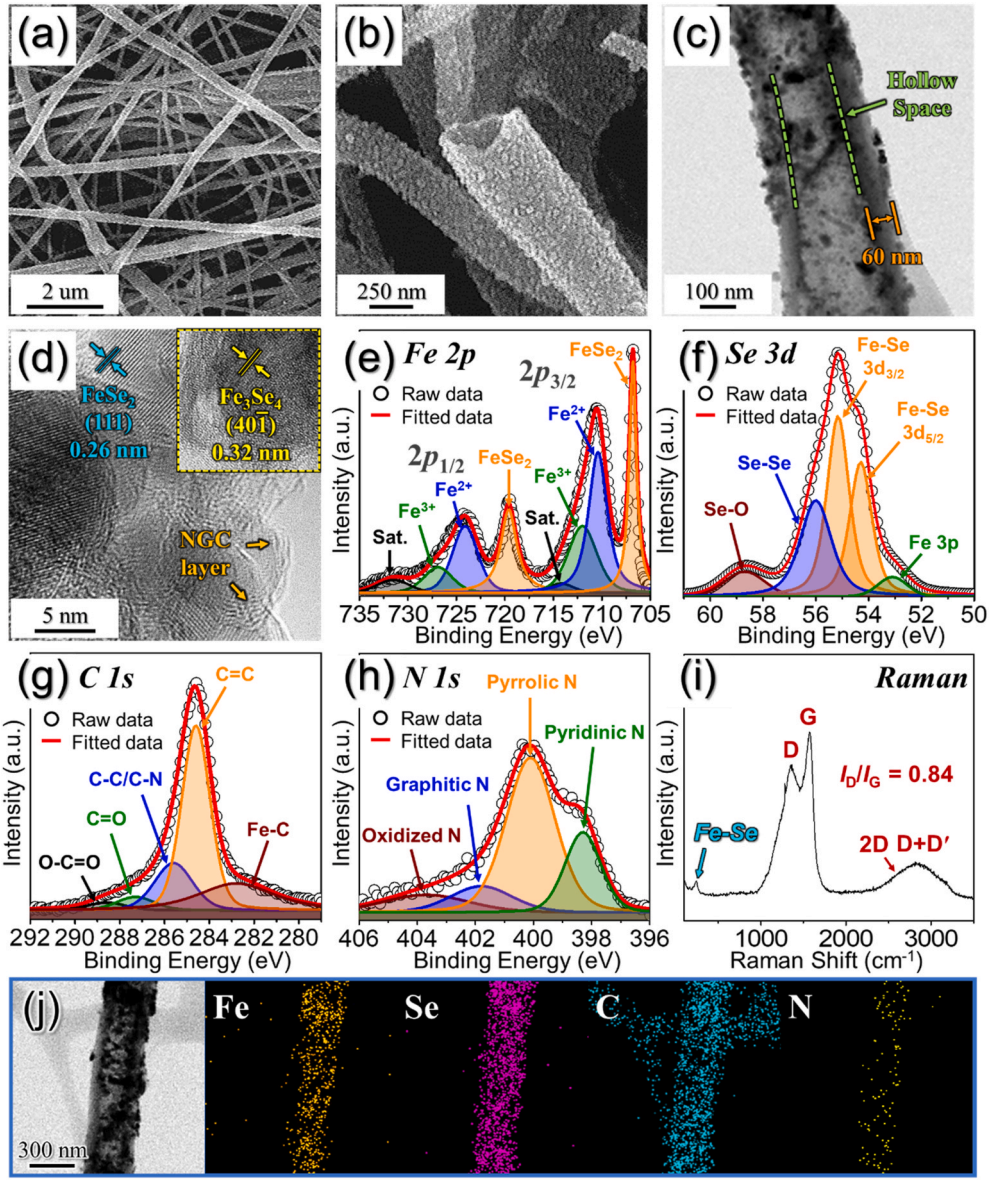

Fig. 2. Physical characterizations of Fe_xSe_y@NGC/rGO HNFs after selenization at 450 °C: (a, b) FE-SEM, (c) TEM, (d) HR-TEM images, (e) Fe 2*p*, (f) Se 3*d*, (g) C 1*s*, (h) N 1*s* XPS spectra, (i) Raman spectrum, and (j) elemental dot mapping images.

rGO NFs—were synthesized and systematically compared with the Fe_xSe_y@NGC/rGO HNFs (Fig. 3). The Fe_xSe_y@NGC/rGO HNFs (Fig. 3a) exhibit a uniform fibrous morphology with well-defined hollow channels and homogeneously distributed nanosized Fe_xSe_y crystallites. This uniformity arises from (i) the high in-plane thermal conductivity of rGO (2000–5000 W m^{-1} K^{-1}), which promotes uniform heat distribution during selenization, and (ii) the hollow channel, which facilitates rapid diffusion of H_2Se gas, ensuring consistent reaction conditions throughout the nanofiber cross-section. In contrast, the rGO-free Fe_xSe_y@NGC HNFs (Fig. 3b) show irregularly grown crystallites protruding from both the fiber exterior and the hollow interior. The absence of rGO reduces lateral heat dissipation, creating localized hot spots that favor uneven nucleation and accelerated crystal coarsening. Similarly, the filled Fe_xSe_y@NGC/rGO NFs (Fig. 3c) exhibit severely enlarged plate-like crystallites on the outer surface. Without an internal diffusion pathway, the fiber core remains shielded from H_2Se gas, leading to a radial temperature gradient and preferential selenization at the surface. These morphological tendencies correlate well with the XRD patterns (Fig. 3d). Both control samples display a more $FeSe_2$-rich biphasic composition compared with the Fe_xSe_y@NGC/rGO HNFs, with the filled architecture showing the strongest $FeSe_2$ dominance. ICP-OES quantification (Table S2) shows that the Fe_xSe_y@NGC/rGO HNFs possess a Fe_3Se_4-rich composition (91.6 mol% Fe_3Se_4), whereas the rGO-free and filled samples contain substantially higher $FeSe_2$ fractions (33.0 and 55.4 mol%, respectively). These results highlight that selenium incorporation strongly depends on the structural environment, where disrupted heat and mass transport in the rGO-free and filled fibers induces excess Se uptake and $FeSe_2$ enrichment, consistent with the non-uniform crystallite overgrowth observed by FE-SEM. EA results (Table S1) provide additional insight. Nitrogen contents are nearly identical (3.2–3.3 wt%) across all samples, as nitrogen originates from PVP. In contrast, carbon contents vary significantly. The rGO-free Fe_xSe_y@NGC HNFs show the lowest carbon content (26.0 wt%) due to the absence of rGO. Although the filled Fe_xSe_y@NGC/rGO NFs contain rGO, their carbon content (28.0 wt%) is lower than that of the Fe_xSe_y@NGC/rGO HNFs (31.6 wt%), which is attributed to their greater $FeSe_2$ fraction—the heavier, Se-rich phase—thereby lowering the normalized carbon wt%. A similar composition-induced effect contributes to the

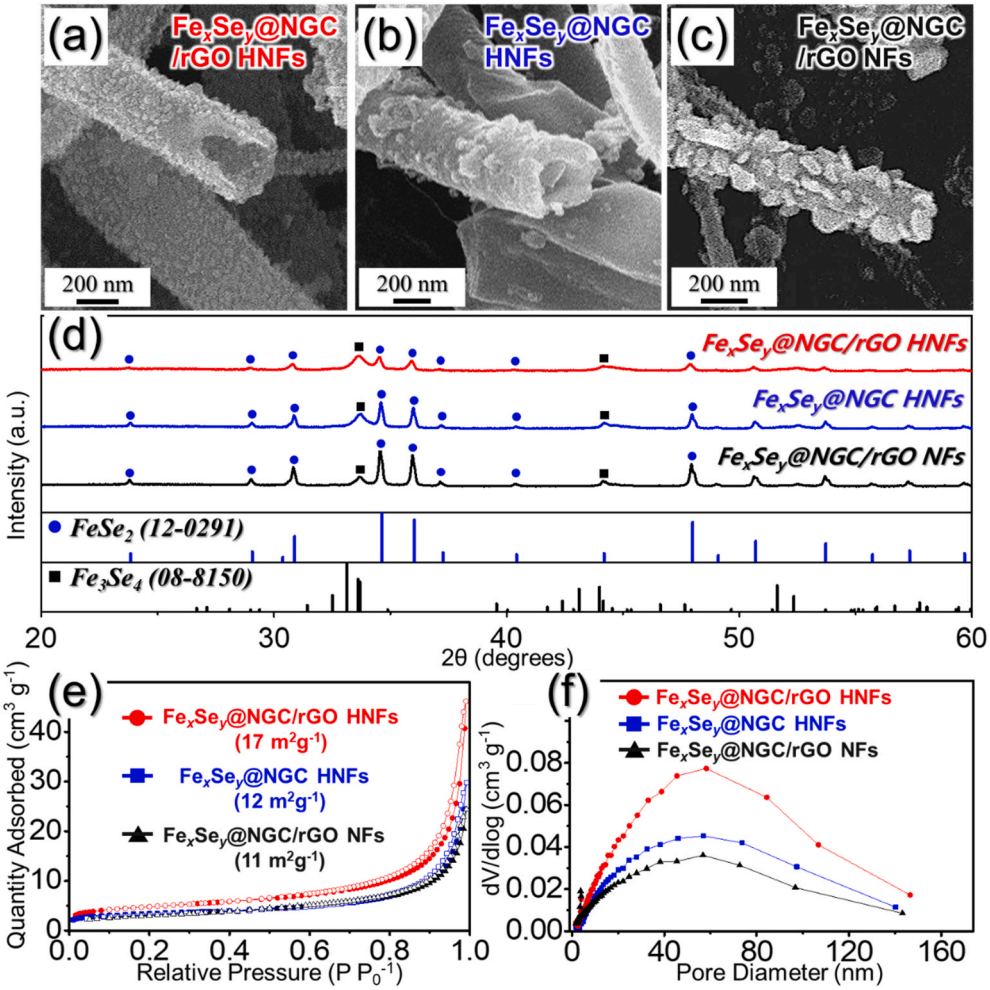

Fig. 3. (a–c) FE-SEM and (d) XRD patterns of Fe_xSe_y@NGC/rGO HNFs, rGO-free Fe_xSe_y@NGC HNFs, and filled Fe_xSe_y@NGC/rGO NFs: (a) Fe_xSe_y@NGC/rGO HNFs, (b) rGO-free Fe_xSe_y@NGC HNFs, (c) filled Fe_xSe_y@NGC/rGO NFs; (e) N_2 adsorption-desorption isotherm and (f) BJH pore-size distribution of Fe_xSe_y@NGC/rGO HNFs, rGO-free Fe_xSe_y@NGC HNFs, and filled Fe_xSe_y@NGC/rGO NFs.

reduced carbon fraction in the rGO-free sample as well. BET analysis (Fig. 3e) further differentiates the architecture. The Fe_xSe_y@NGC/rGO HNFs exhibit the highest surface area (17 m^2 g^{-1}), attributed to the preserved hollow channels and the stabilized fiber framework. This value is comparable to those reported for similar hollow carbon nanofiber-based architectures in previous studies, indicating that the present structure maintains a typical gas-accessible surface area for this class of materials [54,55]. In the rGO-free sample, the surface area decreases to 12 m^2 g^{-1}. This reduction can be attributed to partial coalescence and deformation of the hollow nanofiber framework in the absence of mechanically supportive rGO sheets. Without the structural reinforcement provided by the rGO layers, portions of the hollow fibers tend to collapse or become distorted during thermal treatment, which can obscure parts of the internal hollow channels and reduce the accessible surface area. The filled NFs show the lowest surface area (11 m^2 g^{-1}) due to the absence of internal voids and the presence of overgrown crystallites. BJH pore-size distributions (Fig. 3f) also show minimal accessible pores in the filled fibers. The enlarged surface area and interconnected hollow channels in the Fe_xSe_y@NGC/rGO HNFs promote electrolyte penetration and buffer volume fluctuations during Na-ion cycling, contributing to their superior electrochemical performance.

To evaluate the synergistic effects of the hollow architecture and rGO framework, the electrochemical behaviors of Fe_xSe_y@NGC/rGO HNFs, rGO-free Fe_xSe_y@NGC HNFs, and filled Fe_xSe_y@NGC/rGO NFs were investigated by CV at 0.1 mV s^{-1} in the potential range of 0.01–3.0 V (Fig. 4a and Fig. S7). During the initial cathodic scan, the Fe_xSe_y@NGC/rGO HNFs anode (Fig. 4a) displays multiple reduction features associated with the stepwise Na-storage reactions of the biphasic iron selenides. The first prominent peaks at 1.17 V (Na_xFeSe_2) and 1.10 V ($Na_xFe_3Se_4$) are ascribed to Na-ion intercalation into $FeSe_2$ and Fe_3Se_4, respectively [56–58]. Upon further sodiation, additional reduction peaks at 0.64 and 0.33 V correspond to the conversion of the intercalated phases into FeSe and Na_2Se, followed by their reduction to metallic-Fe, accompanied by the formation of a solid electrolyte interphase (SEI) [56–58]. A small feature near 0.01 V is attributed to Na-ion insertion into the carbon matrix [56–58]. Notably, the intercalation-related peak positions differ among the three electrodes, reflecting distinct degrees of polarization. The Fe_xSe_y@NGC/rGO HNFs exhibit the highest intercalation potential (1.10 V), whereas the rGO-free Fe_xSe_y@NGC HNFs and filled Fe_xSe_y@NGC/rGO NFs show lower values of 0.95 and 1.05 V, respectively (Fig. 4a and Fig. S7). The reduced polarization of the Fe_xSe_y@NGC/rGO HNFs indicates superior charge-transfer kinetics, which can be attributed to the highly conductive rGO network and the continuous hollow structure that collectively facilitate electron and ion transport throughout the hybrid architecture. During the initial anodic scan, multiple oxidation peaks appear, corresponding to the reverse reactions. A small peak at 0.13 V is associated with Na-ion extraction from the carbon matrix, followed by sequential reformation of iron selenides at 1.47 V (FeSe), 1.56 V ($Na_xFe_3Se_4$),

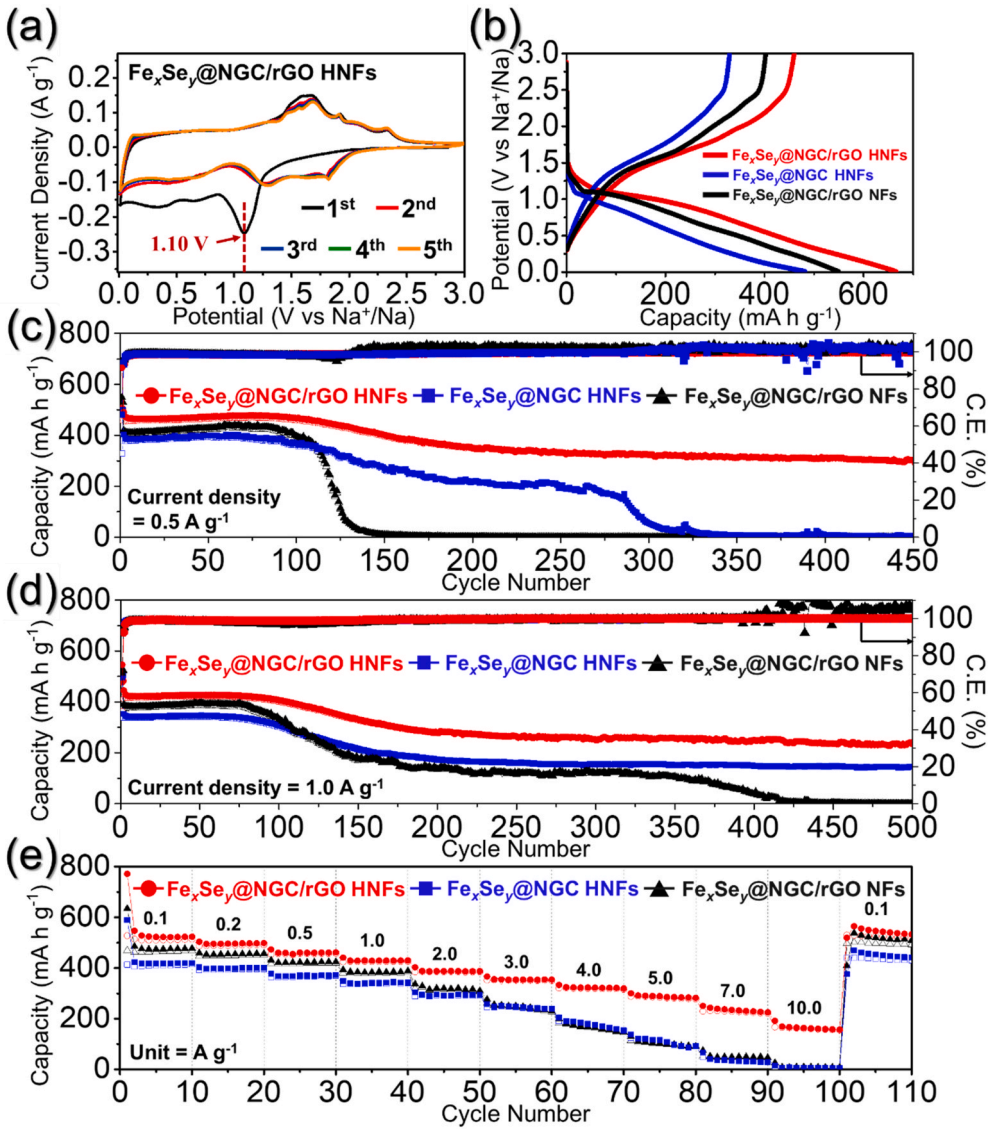

Fig. 4. Electrochemical properties of Fe_xSe_y@NGC/rGO HNFs, rGO-free Fe_xSe_y@NGC HNFs, filled Fe_xSe_y@NGC/rGO NFs: (a) CV curves for initial five cycles Fe_xSe_y@NGC/rGO HNFs, (b) initial Galvanostatic discharge/charge curves at a current density of 0.5 A g^{-1}, (c) cycling performance at 0.5 A g^{-1}, (d) cycling performance at 1.0 A g^{-1}, and (e) rate capabilities.

1.68 V (Na_xFeSe_2), and 1.91 V ($FeSe_2$) [56–58]. The peak at 2.07 V is assigned to the formation of elemental Se, while a broad feature centered at 2.33 V is related to partial SEI decomposition [56–58]. The sharper and more intense oxidation peaks observed for the Fe_xSe_y@NGC/rGO HNFs further confirm its enhanced redox activity and lower kinetic barriers compared with the two control anodes. From the second cycle onward, all electrodes display highly overlapping CV curves, indicating good reversibility. Representative cathodic peaks at 1.63 V (Se sodiation), 1.29 V (Na_xFeSe_2/$Na_xFe_3Se_4$ formation), 0.65 V (FeSe formation), and 0.43 V (metallic-Fe formation) are well preserved, together with an anodic feature at 1.82 V associated with partial SEI reorganization [56–58]. The stable redox profiles of the Fe_xSe_y@NGC/rGO HNFs demonstrate that the combination of rGO-enhanced conductivity and hollow-structure-induced ion-transport facilitation synergistically enables fast reaction kinetics and high reversibility. Based on the above discussion, the overall reaction mechanisms involved in the discharge and charge processes of the Fe_xSe_y@NGC/rGO HNFs can be summarized as follows:

For the discharge and charge process

$$FeSe_2 + xNa^+ + xe^- \leftrightarrow Na_xFeSe_2 \quad (1)$$

$$Fe_3Se_4 + xNa^+ + xe^- \leftrightarrow Na_xFe_3Se_4 \quad (2)$$

$$Na_xFeSe_2 + (2-x)Na^+ + (2-x)e^- \leftrightarrow Na_2Se + FeSe \quad (3)$$

$$Na_xFe_3Se_4 + (8-x)Na^+ + (8-x)e^- \leftrightarrow 4Na_2Se + 3Fe \quad (4)$$

$$FeSe + 2Na^+ + 2e^- \leftrightarrow Na_2Se + Fe \quad (5)$$

$$Na_2Se \leftrightarrow Se + 2Na^+ + 2e^- \quad (6)$$

Initial galvanostatic discharge/charge curves obtained at 0.5 A g^{-1} for all samples are presented in Fig. 4b. The Fe_xSe_y@NGC/rGO HNF anode delivers an initial discharge/charge capacity of 666/460 mA h g^{-1}, corresponding to an initial Coulombic efficiency (ICE) of 69.1%. In comparison, the rGO-free FexSey@NGC HNFs and filled Fe_xSe_y@NGC/rGO NFs exhibit capacities of 482/329 mA h g^{-1} (68.4%) and 549/402 mA h g^{-1} (73.3%), respectively. The variation in ICE reflects the interplay between the structural characteristics of the hollow framework and the presence of rGO. Both hollow-structured samples show moderately lower ICE due to their larger accessible surface areas, which promote electrolyte decomposition during the first cycle.

However, this open architecture is beneficial for long-term cycling stability, as discussed later. Between the two hollow materials, the incorporation of rGO enhances electrical conductivity and partially suppresses parasitic reactions, giving the Fe_xSe_y@NGC/rGO HNFs a slightly higher ICE than the rGO-free counterpart. Meanwhile, the filled Fe_xSe_y@NGC/rGO NFs exhibit the highest ICE because their limited surface area minimizes initial SEI formation. The initial discharge/charge polarization values (Fig. S8) further highlight these kinetic differences. The Fe_xSe_y@NGC/rGO HNFs exhibit the smallest polarization ($\Delta V = 0.75$ V), demonstrating the synergistic effects of rGO-assisted electron transport and the hollow interior that ensures uniform Na-ion access to the active material. The filled Fe_xSe_y@NGC/rGO NFs show a moderate polarization ($\Delta V = 0.83$ V), benefitting from enhanced electronic conductivity but hindered by restricted ion pathways. In contrast, the rGO-free Fe_xSe_y@NGC HNFs display the largest polarization ($\Delta V = 0.89$ V) due to limited conductivity and non-uniform reaction environments. These findings align well with the CV analysis, where the Fe_xSe_y@NGC/rGO HNFs exhibit the sharpest and least-shifted redox peaks among the three samples. Overall, the initial voltage profiles and polarization characteristics clearly demonstrate that the combined effects of the hollow structure and rGO framework significantly enhance Na-ion storage kinetics and promote more effective utilization of the biphasic Fe_xSe_y active material.

Long-term cycling performance was further evaluated at 0.5 and 1.0 A g^{-1} (Fig. 4c and d), and all three anodes exhibited consistent capacity-ordering trends across both current densities. In the early stage of cycling (<100 cycles), the filled Fe_xSe_y@NGC/rGO NFs deliver a higher capacity than the rGO-free Fe_xSe_y@NGC HNFs, mainly due to their $FeSe_2$-rich composition and the presence of rGO, which together enhance the initial Na-storage kinetics. However, this advantage rapidly disappears as cycling proceeds. Because the filled architecture lacks internal void space to buffer the substantial volume fluctuations inherent to repeated conversion reactions, it undergoes accelerated structural degradation, leading to nearly complete capacity loss within 150 cycles at 0.5 A g^{-1}. In contrast, the rGO-free Fe_xSe_y@NGC HNFs exhibit better long-term stability than the filled counterpart, despite their lower initial capacity. This improvement arises from the hollow interior, which provides mechanical compliance and mitigates pulverization. Nevertheless, the absence of rGO restricts electronic conductivity and weakens structural integrity, ultimately resulting in performance degradation beyond 350 cycles at 0.5 A g^{-1}. Among the three architectures, the Fe_xSe_y@NGC/rGO HNFs demonstrate the most balanced behavior—high initial capacity combined with exceptional structural resilience—stemming from the synergistic effects of the hollow framework and the rGO network. The hollow channels shorten Na-ion diffusion distances and accommodate conversion-induced volume changes, while the rGO framework enhances electron transport and reinforces the carbon matrix. As a result, the Fe_xSe_y@NGC/rGO HNFs retain 303 mA h g^{-1} after 450 cycles at 0.5 A g^{-1} with a low average decay rate of only 0.38 mA h g^{-1} per cycle, whereas both control samples suffer nearly complete capacity fading over the same period. The same capacity-ordering (Fe_xSe_y@NGC/rGO HNFs > rGO-free Fe_xSe_y@NGC HNFs > filled Fe_xSe_y@NGC/rGO NFs) and degradation behaviors persist at 1.0 A g^{-1} (Figs. 4d) and 2.0 A g^{-1} (Fig. S9). Even under these harsher conditions, the Fe_xSe_y@NGC/rGO HNFs maintain outstanding reversibility, delivering 235 mA h g^{-1} after 500 cycles at 1.0 A g^{-1} (CE = 99.9%) and 290 mA h g^{-1} after 100 cycles at 2.0 A g^{-1} (CE = 98.3%). Collectively, these results demonstrate that the simultaneous presence of rGO and the hollow architecture enables both high capacity and durable electro-chemo-mechanical stability, confirming the structural advantages of the Fe_xSe_y@NGC/rGO HNFs under prolonged Na-ion cycling. A noticeable capacity decay is observed around 120 cycles (Fig. 4c and d), which is further analyzed using differential capacity (dQ/dV) curves, post-cycling CV profile (Fig. S10), and post-cycling structural characterizations (Fig. S11). The dQ/dV profiles reveal that several peaks associated with Se-related reactions gradually decrease and eventually disappear with increasing cycle numbers. In particular, the peaks located at 2.07 and 2.33 V (Se formation and partial SEI decomposition) and their corresponding reduction peaks (1.80 and 1.63 V, Se sodiation) progressively weaken, indicating the occurrence of irreversible reactions involving Se-species. This behavior suggests that a portion of Se generated during the initial conversion reactions undergoes gradual dissolution into the electrolyte, leading to capacity fading. *Ex-situ* FE-SEM and TEM analyses at intermediate cycle numbers (50 and 120 cycles, Fig. S11) show that the overall fibrous morphology and hollow architecture are well preserved, confirming the structural robustness of the composite during cycling. HR-TEM images reveal the presence of Se lattice fringes (0.38 nm), indicating the formation of intermediate Se phases. In addition, SAED patterns show that the diffraction rings corresponding to Se gradually weaken with increasing cycle number, which is consistent with the evolution of the dQ/dV profiles and supports the progressive loss of Se-species. Despite this partial Se dissolution, the redox peaks associated with the reversible conversion of Fe_xSe_y remain well maintained even after extended cycling (Fig. S10a), indicating that the main active framework is preserved. Therefore, the temporary capacity decay around ~120 cycles originates from irreversible Se-related reactions, while the stable long-term performance is enabled by the structurally robust hollow NGC/rGO framework. In addition to understanding the origin of the capacity decay, the practical applicability of the anode was further evaluated under higher mass loading conditions of approximately 1.3, 1.5, and 2.0 mg cm^{-2} (Fig. S12). The anode with a mass loading of 1.3 mg cm^{-2} delivered a reversible capacity of approximately 444 mA h g^{-1} after 100 cycles at a current density of 0.5 A g^{-1}. When the loading was increased to 1.5 mg cm^{-2}, the anode still maintained a comparable capacity of about 396 mA h g^{-1} with stable cycling behavior. Even at a higher loading of 2.0 mg cm^{-2}, the anode exhibited a reversible capacity of approximately 372 mA h g^{-1} after 100 cycles, demonstrating good capacity retention. Although a gradual decrease in specific capacity is observed with increasing mass loading, this behavior can be attributed to increased ion diffusion resistance and extended Na-ion transport pathways within thicker electrodes. Nevertheless, the electrode maintains stable cycling performance even at 2.0 mg cm^{-2}, indicating that the hollow NGC/rGO framework effectively preserves electrochemical stability and efficient charge transport under relatively high loading conditions.

Rate capability was evaluated across a wide current density range from 0.1 to 10.0 A g^{-1} (Fig. 4e). The Fe_xSe_y@NGC/rGO HNFs exhibit the best rate performance among all samples, delivering discharge capacities of 523, 499, 462, 430, 388, 354, 320, 282, 225, and 157 mA h g^{-1} at 0.1, 0.2, 0.5, 1.0, 2.0, 3.0, 4.0, 5.0, 7.0, and 10.0 A g^{-1}, respectively. Upon returning the current density to 0.1 A g^{-1}, the capacity recovers to 533 mA h g^{-1}, nearly identical to the initial value, confirming excellent rate reversibility and structural integrity. A clear performance hierarchy is observed. Up to 1.0 A g^{-1}, the capacity follows the order Fe_xSe_y@NGC/rGO HNFs > Fe_xSe_y@NGC/rGO NFs > Fe_xSe_y@NGC HNFs, reflecting trends consistent with long-term cycling. The filled Fe_xSe_y@NGC/rGO NFs benefit from rGO and their relatively high $FeSe_2$ content, producing 478, 457, 425, and 389 mA h g^{-1} at 0.1–1.0 A g^{-1}. However, at higher current densities (>1.0 A g^{-1}), their capacity rapidly deteriorates to 310, 230, 148, 91, 47, and 8 mA h g^{-1} at 2.0–10.0 A g^{-1}. This steep decline arises from their filled morphology, which lacks sufficient free volume to buffer conversion-induced stresses during rapid Na-ion cycling. The rGO-free Fe_xSe_y@NGC HNFs display the lowest rate performance across all current densities, delivering 420–343 mA h g^{-1} at 0.1–1.0 A g^{-1} and sharply decreasing to 294, 239, 154, 92, 28, and 5 mA h g^{-1} at 2.0–10.0 A g^{-1}. Although the hollow interior provides some accommodation for volume changes, the absence of rGO results in limited electronic conductivity and non-uniform reaction propagation, both of which accelerate capacity fading at high rates. In stark contrast, only the Fe_xSe_y@NGC/rGO HNFs maintain high and reversible capacities throughout the full current density range. Their superior rate

capability stems from the synergistic combination of shortened ion-diffusion pathways provided by the hollow channels and rapid electron transport enabled by the rGO scaffold. Together, these features ensure efficient Na-ion access and stable electro-chemo-mechanical behavior even under demanding conditions. Comparison with recently reported iron selenide anodes (Table S3) further highlights that the present Fe_xSe_y@NGC/rGO HNFs match or surpass state-of-the-art materials in both high-rate performance and long-term durability, underscoring the effectiveness of the proposed structural design.

To further evaluate the reaction kinetics of the Fe_xSe_y@NGC/rGO HNFs anode, CV measurements were performed at scan rates ranging from 0.1 to 2.0 mV s^{-1} (Fig. 5a). The CV profiles retain their overall shape even at the highest scan rate, indicating highly reversible and fast redox processes. The charge storage mechanism was analyzed by examining the dependence of peak current (i) on the scan rate (ν), which follows the power-law relationship [59]:

$$i = a\nu^b \tag{7}$$

$$\log(i) = \log(a) + b\log(\nu) \tag{8}$$

A b-value of 0.5 corresponds to a diffusion-controlled process, whereas a value approaching 1.0 signifies a capacitive-dominated mechanism [59]. As shown in Fig. 5b, both anodic and cathodic peaks yield b-values close to unity, demonstrating that Na-ion storage in the Fe_xSe_y@NGC/rGO HNFs is predominantly governed by capacitive processes. To further quantify the pseudocapacitive contribution, the CV data were analyzed using the following equation [60]:

$$i = k_1\nu + k_2\nu^{1/2} \tag{9}$$

where the $k_1\nu$ corresponds to capacitive response and the $k_2\nu^{1/2}$ represents diffusion-controlled behavior [60]. The extracted capacitive fractions (Fig. 5c) reveal a dominant pseudocapacitive contribution of 93% at 2.0 mV s^{-1}, progressively increasing from 72% to 93% as the scan rate increases from 0.1 to 2.0 mV s^{-1} (Fig. 5d). This high capacitive contribution is primarily attributed to the ultrafine size of the Fe_xSe_y nanocrystals, as shown in Fig. S5. Such a drastic reduction in crystal size significantly increases the surface-to-volume ratio, providing a vast number of electrochemically active sites for surface-induced Na-ion storage. These findings are consistent with recent reports on nanoscale iron selenides, which exhibit capacitive contributions exceeding 90% at high scan rates [61–64]. The strong pseudocapacitive character of the Fe_xSe_y@NGC/rGO HNFs also originates from their hierarchical architecture: the hollow channels provide rapid electrolyte penetration and abundant accessible surface sites, while the rGO framework ensures fast electron transport throughout the network. Together, these features promote accelerated surface redox reactions and efficient charge transfer, resulting in a dominant capacitive response across a wide range of scan rates.

Further kinetic verification was conducted through EIS analysis to elucidate interfacial charge-transfer behavior and Na-ion diffusion during cycling. EIS measurements were collected for fresh anodes, after the 1st cycle, and after the 300th cycle at 1.0 A g^{-1} (Fig. 6a–c and S13), and the corresponding fitting results based on a Randles-type equivalent circuit (Fig. S14) are summarized in Table S4. In the fresh state (Fig. 6a), the Fe_xSe_y@NGC/rGO HNFs exhibit the lowest electrolyte resistance (R_e = 14 Ω), indicating efficient electrolyte penetration enabled by the hollow channels. The initial R_{ct} varies significantly among the samples. The rGO-free Fe_xSe_y@NGC HNFs show the highest R_{ct} (1290 Ω) due to the absence of a conductive carbon nanosheet network and the enlarged interfacial area associated with the hollow structure. In contrast, the filled Fe_xSe_y@NGC/rGO NFs show a lower R_{ct} (601 Ω), not only because of the presence of rGO but also their compact morphology, which shortens interparticle charge-transfer pathways and reduces the number of initially active interfaces. The Fe_xSe_y@NGC/rGO HNFs display an intermediate R_{ct} (679 Ω), as the increased interfacial area from the hollow architecture is offset by the high electronic conductivity

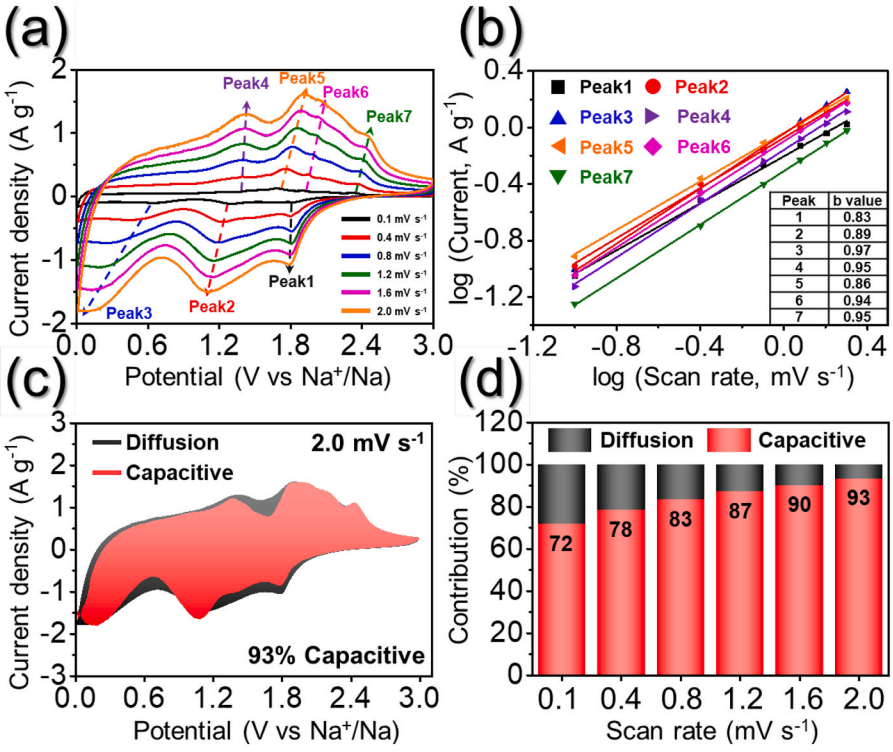

Fig. 5. Electrochemical reaction dynamics analysis of (a–d) Fe_xSe_y@NGC/rGO HNFs: (a) CV curves obtained at various scan rates, (b) current response (i) *vs.* scan rate (n) at each redox peak, (c) CV curves with the capacitive fraction shown by the red region at a scan rate of 2.0 mV s^{-1}, and (d) bar chart showing the percentage of the capacitive contribution at different scan rates. (For interpretation of the references to colour in this figure legend, the reader is referred to the Web version of this article.)

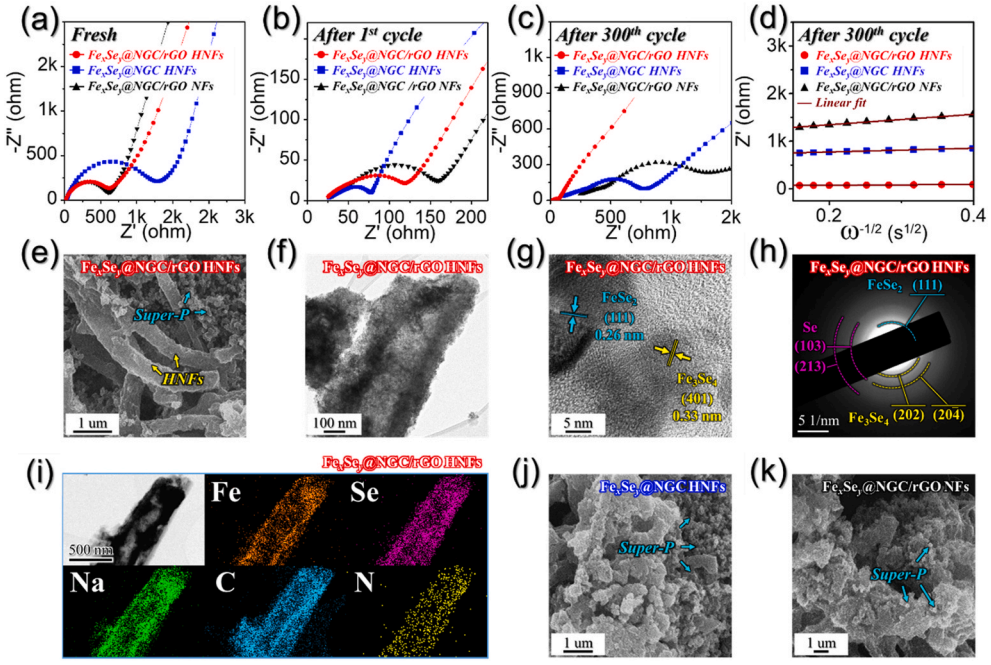

Fig. 6. (a–d) Nyquist impedance plots and (e–k) post-cycling structural characterization of Fe_xSe_y@NGC/rGO HNFs, rGO-free Fe_xSe_y@NGC HNFs, and filled Fe_xSe_y@NGC/rGO NFs after 300th cycle: (a) fresh state, (b) after 1st cycle, (c) after 300th cycle, (d) relationships between the real part of the impedance (Z_{re}) and $\omega^{-1/2}$ obtained after 300 cycles at 0.5 A g^{-1}, (e) FE-SEM image, (f) TEM image, (g) HR-TEM image, (h) SAED pattern, (i) elemental mapping images of FexSey@NGC/rGO HNFs, (f) FE-SEM image of rGO-free Fe_xSe_y@NGC HNFs, and (g) FE-SEM image of filled Fe_xSe_y@NGC/rGO NFs after 300 cycles at 0.5 A g^{-1}.

imparted by the rGO scaffold. This balance results in a moderate initial R_{ct}, which evolves favorably as cycling progresses and more electrochemically active pathways become accessible. After the 1st cycle (Fig. 6b), all anodes show a pronounced decrease in R_{ct}, attributed to the formation of ultrafine amorphous intermediates and stabilization of the SEI layer, both of which facilitate Na-ion insertion/extraction [65]. However, long-term cycling reveals a clear divergence in impedance evolution (Fig. 6c). The Fe_xSe_y@NGC/rGO HNFs maintain the lowest R_{ct} (50 Ω) after 300 cycles, demonstrating that their hybrid NGC/rGO conductive network and hollow structure effectively preserve rapid charge-transfer kinetics. Their low R_e (23 Ω) and R_f (53 Ω) further confirm that the electrolyte interface and SEI layer remain structurally intact and electronically percolating over prolonged operation. In contrast, the rGO-free Fe_xSe_y@NGC HNFs exhibit severe increases in R_e (24 to 236 Ω) and R_f (694 Ω), indicative of structural collapse, fragmentation, and SEI destabilization. The filled Fe_xSe_y@NGC/rGO NFs deteriorate even more dramatically, with R_e increasing from 27 to 399 Ω and R_f reaching 988 Ω, evidencing progressive interfacial blockage and insufficient stress accommodation. These impedance increases strongly correlate with their rapid capacity fading (Fig. 4c and d), confirming that compact, non-hollow architectures cannot sustain volume fluctuations associated with repeated conversion reactions.

Na-ion diffusion coefficients (D_{Na^+}) were subsequently calculated using the Warburg impedance factor (σ_w) derived from the relationship $Z' = R_s + R_{ct} + \sigma_w \omega^{-1/2}$ (Fig. 6d). As observed, the Fe_xSe_y@NGC/rGO HNFs anode exhibits the least steep slope, indicating higher D_{Na^+} due to its highly conductive and porous nanostructure. The D_{Na^+} values were obtained using the following equation [66]:

$$D = R^2T^2 / 2A^2F^4C^2\sigma_w^2 \quad (10)$$

where R is the gas constant, T is the temperature, A is the surface area of electrode, C is the molar concentration of Na-ion, F is the Faraday constant, and σ_w is the Warburg coefficient. The Fe_xSe_y@NGC/rGO HNFs anode exhibits the highest D_{Na^+} (1.67×10^{-12} cm^2 s^{-1}), exceeding those of the rGO-free Fe_xSe_y@NGC HNFs (9.68×10^{-14} cm^2 s^{-1}) and filled Fe_xSe_y@NGC/rGO NFs (1.17×10^{-14} cm^2 s^{-1}) by approximately two orders of magnitude. This superior diffusion behavior of the Fe_xSe_y@NGC/rGO HNFs arises from the hollow nanochannel facilitating ion transport and the rGO-supported conductive network maintaining electronic pathways during long-term operation. Post-cycling morphological analyses (Fig. 6e–k) further corroborate the impedance findings. As shown in Fig. 6e, the Fe_xSe_y@NGC/rGO HNFs retain their fibrous morphology after 300 cycles, indicating excellent structural stability. More importantly, *ex-situ* TEM analysis (Fig. 6f) reveals that the hollow interior remains well preserved without being fully filled by SEI or pulverized products, confirming that the internal nanochannels remain accessible during prolonged cycling. HR-TEM images (Fig. 6g) further demonstrate that the biphasic iron selenide nanocrystals remain well anchored to the carbon matrix. Clear lattice fringes corresponding to $FeSe_2$ and Fe_3Se_4 are observed even after 300 cycles, indicating that the main active framework is structurally stable. As discussed above, in contrast to earlier cycles (Figs. S10 and S11), the Se-related features become significantly weakened after prolonged cycling, suggesting gradual Se loss due to partial dissolution into the electrolyte during repeated sodiation/de-sodiation processes. The corresponding SAED pattern (Fig. 6h) confirms the preservation of the crystalline $FeSe_2$ and Fe_3Se_4 phases, while the diffraction rings associated with Se become less pronounced, further supporting the progressive loss of Se. Elemental mapping images (Fig. 6i) shows a uniform distribution of Fe, Se, C, N, and Na throughout the nanofiber structure. The detected Na originates from residual SEI components, and its homogeneous distribution suggests that the SEI layer is conformal rather than blocking the hollow interior. In contrast, the rGO-free Fe_xSe_y@NGC HNFs (Fig. 6j) exhibit severe pulverization and aggregation after prolonged cycling, while the filled Fe_xSe_y@NGC/rGO NFs (Fig. 6k) suffer from significant structural collapse and cracking. Collectively, these results clearly demonstrate that only the hollow NGC/rGO framework can effectively maintain structural integrity and electrochemical functionality during long-term cycling.

To further explore the practical feasibility of the Fe_xSe_y@NGC/rGO HNFs, a P2-type layered $Na_{0.67}(Mn_{0.5}Ni_{0.333}Fe_{0.167})O_2$ (NMNF) cathode

was synthesized and evaluated. Prior to full-cell assembly, the electrochemical performance of the NMNF cathode was validated in a Na-ion half-cell configuration (Fig. S15). The cathode delivered a stable discharge capacity of approximately 100 mA h g^{-1} after 100 cycles at 0.5C (1.0C = 173 mA h g^{-1}) and exhibited excellent rate tolerance, maintaining 76 mA h g^{-1} even at a high current density of 5.0C. These results confirm that the synthesized NMNF cathode provides a reliable and kinetically stable platform for evaluating the full-cell performance. Subsequently, full-cells were assembled with a capacity ratio between the anode and cathode (N/P ratio) of 1.2 and operated within a wide voltage range of 0.5–4.5 V (Fig. 7a). The NMNF||Fe_xSe_y@NGC/rGO HNFs full-cell successfully powered a 5 V light-emitting diode (LED) (Fig. 7b) and delivered a high reversible capacity of approximately 143 mA h g^{-1} at 0.1C (based on the cathode mass). During cycling performance at 0.5C (Fig. 7c), the full-cell maintained a specific capacity of 95 mA h g^{-1} after 100 cycles, corresponding to a capacity retention of 73%. Notably, this retention trend mirrors the intrinsic cycling stability of the NMNF cathode observed in half-cell tests, suggesting that the capacity decay of full-cell is primarily cathode-limited. This result confirms that the Fe_xSe_y@NGC/rGO HNFs can stably and reversibly host the Na-ions oscillating from the cathode framework throughout extended cycling. Furthermore, rate capability tests (Fig. 7d) highlighted the robust kinetics of the integrated architecture, where the anode component maintained a substantial capacity of 73 mA h g^{-1} (based on cathode mass) even at an elevated rate of 5.0C. Such kinetic resilience reflects the efficient charge-transfer and rapid Na-ion transport facilitated by the 1D hollow architecture, underscoring the potential of Fe_xSe_y@NGC/rGO HNFs as a high-performance anode for practical Na-ion batteries.

4. Conclusions

In summary, a sublimation-induced synthesis strategy was developed to construct N-doped graphitic carbon/reduced graphene oxide hybrid hollow nanofibers hosting biphasic iron selenide nanocrystals (Fe_xSe_y@NGC/rGO HNFs). Camphene sublimation during electrospinning generated well-defined longitudinal hollow channels that enabled rapid electrolyte infiltration, shortened Na-ion diffusion pathways, and effectively buffered the large volume changes accompanying conversion reactions. Controlled selenization subsequently produced a uniformly dispersed $FeSe_2$/Fe_3Se_4 biphasic mixture encapsulated within an NGC layer and interconnected through a conductive rGO framework, yielding an electro-chemo-mechanically robust architecture. The coexistence of $FeSe_2$ and Fe_3Se_4 provided complementary advantages—high capacity and enhanced electronic conductivity—while the dual-carbon scaffold ensured efficient charge transport and preserved structural integrity over prolonged cycling. As a result, the Fe_xSe_y@NGC/rGO HNF anode delivered exceptional Na-ion storage performance, including high-rate capability up to 10.0 A g^{-1} and remarkable long-term cycling stability at 0.5–2.0 A g^{-1}, outperforming both rGO-free and non-hollow control anodes. Collectively, these findings demonstrate that sublimation-engineered hollow carbon architectures combined with phase-engineered metal selenide hosts offer a powerful design platform for next-generation high-performance SIB anodes.

CRediT authorship contribution statement

Jae Seob Lee: Conceptualization, Formal analysis, Methodology, Visualization, Writing – original draft, Writing – review & editing. **Ji Hun Baek:** Data curation, Formal analysis, Investigation, Validation, Visualization. **Rakesh Saroha:** Writing – original draft. **Jae-Oh Shim:** Formal analysis, Validation. **Chungyeon Cho:** Formal analysis, Investigation. **Sang Mun Jeong:** Resources. **Gi Dae Park:** Writing – review & editing. **Yun Chan Kang:** Funding acquisition, Resources. **Jung Sang Cho:** Funding acquisition, Project administration, Resources,

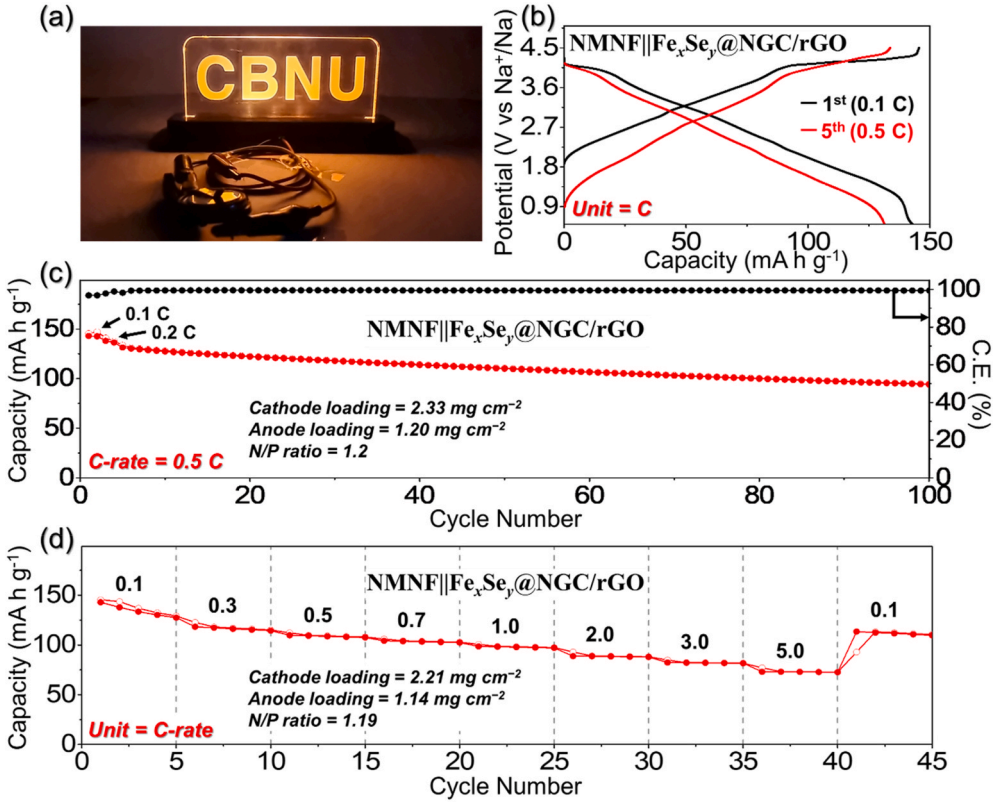

Fig. 7. (a) Digital image of a light-emitting diode (5 V, 10 mW) powered by one full-cell consisting of $Na_{0.67}(Mn_{0.5}Ni_{0.333}Fe_{0.167})O_2$ (NMNF) cathode and Fe_xSe_y@NGC/rGO HNFs anode utilized after fully charging at 0.1C (1.0C = 173 mA g^{-1}), (b) initial Galvanostatic charge/discharge curves at current densities of 0.1C and 0.5C, (c) cycling performance at 0.5C, and (d) rate capability test.

Supervision, Writing – review & editing.

Declaration of competing interest

The authors declare that they have no known competing financial interests or personal relationships that could have appeared to influence the work reported in this paper.

Acknowledgments

This work was supported by the National Research Foundation of Korea (NRF) grant funded by the Korea government (MSIT) (RS-2025-00556955 and RS-2023-00217581). This work was supported by the Korea Institute of Energy Technology Evaluation and Planning (KETEP) and the Ministry of Trade, Industry & Energy (MOTIE) of the Republic of Korea (No. RS-2024-00394769).

Appendix A. Supplementary data

Supplementary data to this article can be found online at https://doi.org/10.1016/j.jpowsour.2026.240179.

Data availability

No data was used for the research described in the article.

References

[1] J.S. Lee, D.G. Ryu, R. Saroha, S.W. Cho, G.D. Park, C. Cho, J.S. Cho, Polydopamine-derived carbon-coated reduced graphene oxide microspheres comprising layered double hydroxide-derived binary metal selenide nanocrystals as high-performance anodes for sodium-ion batteries, J. Alloys Compd. 1037 (2025) 182406, https://doi.org/10.1016/j.jallcom.2025.182406.

[2] X. Yang, A.L. Rogach, Anodes and sodium-free cathodes in sodium ion batteries, Adv. Energy Mater. 10 (22) (2020) 2000288, https://doi.org/10.1002/aenm.202000288.

[3] T. Zhang, C. Li, F. Wang, A. Noori, M.F. Mousavi, X. Xia, Y. Zhang, Recent advances in carbon anodes for sodium-ion batteries, Chem. Rec. 22 (10) (2022) e202200083, https://doi.org/10.1002/tcr.202200083.

[4] S.W. Cho, H.H. Choi, T.G. Senthamaraikannan, D.H. Lim, G.D. Park, C. Cho, S. M. Jeong, R. Saroha, J.S. Cho, Hierarchical porous one-dimensional N-doped C framework comprising ultrafine Mo_2C catalysts for stable Na/K–Se batteries: experimental and theoretical investigations, Chem. Eng. J. 512 (2025) 162456, https://doi.org/10.1016/j.cej.2025.162456.

[5] J. Wang, L. Xi, C. Peng, X. Song, X. Wan, L. Sun, M. Liu, J. Liu, Recent progress in hard carbon anodes for sodium-ion batteries, Adv. Eng. Mater. 26 (8) (2024) 2302063, https://doi.org/10.1002/adem.202302063.

[6] F. Xie, L. Zhang, C. Ye, M. Jaroniec, S.Z. Qiao, The application of hollow structured anodes for sodium-ion batteries: from simple to complex systems, Adv. Mater. (38) (2019) 1800492, https://doi.org/10.1002/adma.201800492.

[7] S.-M. Zheng, Y.-R. Tian, Y.-X. Liu, S. Wang, C.-Q. Hu, B. Wang, K.-M. Wang, Alloy anodes for sodium-ion batteries, Rare Met. 40 (2021) 272–289, https://doi.org/10.1007/s12598-020-01605-z.

[8] T. Perveen, M. Siddiq, N. Shahzad, R. Ihsan, A. Ahmad, M.I. Shahzad, Prospects in anode materials for sodium ion batteries-A review, Renew. Sustain. Energy Rev. 119 (2020) 109549, https://doi.org/10.1016/j.rser.2019.109549.

[9] J.S. Lee, J.-S. Park, K.W. Baek, R. Saroha, S.H. Yang, Y.C. Kang, J.S. Cho, Coral-like porous microspheres comprising polydopamine-derived N-doped C-coated $MoSe_2$ nanosheets composited with graphitic carbon as anodes for high-rate sodium-and potassium-ion batteries, Chem. Eng. J. 456 (2023) 141118, https://doi.org/10.1016/j.cej.2022.141118.

[10] S.C. Lee, Y.H. Kim, J.H. Park, D. Susanto, J.Y. Kim, J. Han, S.C. Jun, K.Y. Chung, Mechanical activation of graphite for Na-Ion battery anodes: unexpected reversible reaction on solid electrolyte interphase via x-ray analysis, Adv. Sci. 11 (28) (2024) 2401022, https://doi.org/10.1002/advs.202401022.

[11] Z.-L. Xu, G. Yoon, K.-Y. Park, H. Park, O. Tamwattana, S. Joo Kim, W.M. Seong, K. Kang, Tailoring sodium intercalation in graphite for high energy and power sodium ion batteries, Nat. Commun. 10 (2019) 2598, https://doi.org/10.1038/s41467-019-10551-z.

[12] L. Habib, G. Suo, J. Li, C. Lin, X. Luo, G. Yang, Z.K. Kalkozova, K. Naseem, Interface and structural modulation stabilization strategies for layered transition metal oxide cathodes in sodium-ion batteries, Energy Storage Mater. 84 (2026) 104863, https://doi.org/10.1016/j.ensm.2025.104863.

[13] J.S. Lee, R. Saroha, J.S. Cho, Porous microspheres comprising $CoSe_2$ nanorods coated with N-Doped graphitic C and polydopamine-derived C as anodes for long-lived Na-Ion batteries, Nano-Micro Lett. 14 (2022) 113, https://doi.org/10.1007/s40820-022-00855-z.

[14] J.S. Lee, R. Saroha, S.H. Oh, D.H. Shin, S.M. Jeong, J.K. Kim, J.S. Cho, Rational design of perforated bimetallic (Ni, Mo) sulfides/N-doped graphitic carbon composite microspheres as anode materials for superior Na-Ion batteries, Small Methods 5 (9) (2021) 2100195, https://doi.org/10.1002/smtd.202100195.

[15] P. Muthu, S. Rajagopal, D. Saju, V. Kesavan, A. Dellus, L. Sadhasivam, N. Chandrasekaran, Review of transition metal chalcogenides and halides as electrode materials for thermal batteries and secondary energy storage systems, ACS Omega 9 (7) (2024) 7357–7374, https://doi.org/10.1021/acsomega.3c08809.

[16] S. Palchoudhury, K. Ramasamy, J. Han, P. Chen, A. Gupta, Transition metal chalcogenides for next-generation energy storage, Nanoscale Adv. 5 (10) (2023) 2724–2742, https://doi.org/10.1039/d2na00944g.

[17] L. Li, S. Wang, J. Peng, J. Lai, H. Zhang, J. Yang, Transition metal selenide-based anodes for advanced sodium-ion batteries: electronic structure manipulation and heterojunction construction aspect, Molecules 29 (13) (2024) 3083, https://doi.org/10.3390/molecules29133083.

[18] L. Wang, K. Bai, Y. Lu, W. Mo, L. Zhang, Controllable hierarchical porous $FeSe_2$ with excellent long cycle lifespan as anode materials for sodium-ion battery, J. Power Sources 592 (2024) 233913, https://doi.org/10.1016/j.jpowsour.2023.233913.

[19] M. Ren, H. Zang, S. Cao, W. Liu, M. Li, J. Yao, F. Cai, J. Cui, Y. Wang, Fe_3Se_4 decorating carbon nanotubes with superior sodium storage performance for sodium-ion batteries, J. Energy Storage 81 (2024) 110486, https://doi.org/10.1016/j.est.2024.110486.

[20] J. Lin, L. Shao, S. Wang, S. Zhou, L. Yu, X. Shi, J. Xu, Z. Sun, H. Pan, Nitrogen-doped carbon-modified Fe_3Se_4 as high pseudocapacitive anode for fast sodium-ion storage, J. Energy Storage 139 (2025) 118818, https://doi.org/10.1016/j.est.2025.118818.

[21] G. Li, B. Zhang, J. Rao, D.H. Gonzalez, G.R. Blake, R.A. Groot, T.T.M. Palstra, Effect of vacancies on magnetism, electrical transport, and thermoelectric performance of marcasite $FeSe_{2-\delta}$ ($\delta = 0.05$), Chem. Mater. 27 (24) (2015) 8220–8229, https://doi.org/10.1021/acs.chemmater.5b03562.

[22] S.J. Yadav, I.A. Shaikh, S. Sahoo, D.V. Shah, Investigating the structural and magnetic properties of Fe_3Se_4 nanoparticles and it's photocatalytic application, Phys. B Condens. Matter 691 (2024) 416358, https://doi.org/10.1016/j.physb.2024.416358.

[23] Y. Zhang, Q. Zhou, J. Zhu, Q. Yan, S.X. Dou, W. Sun, Nanostructured metal chalcogenides for energy storage and electrocatalysis, Adv. Funct. Mater. 27 (35) (2017) 1702317, https://doi.org/10.1002/adfm.201702317.

[24] Y. Pan, X. Cheng, L. Gong, L. Shi, Y. Deng, H. Zhang, Highly reversible Na ion storage in N-doped polyhedral carbon-coated transition-metal chalcogenides by optimizing the nanostructure and surface engineering, J. Mater. Chem. A 6 (2018) 18967–18978, https://doi.org/10.1039/c8ta07790h.

[25] L. Zhang, X. Li, L. Tai, C. Shen, J. Yang, C. Sun, H. Geng, X. Zuo, Constructing electronic interconnected bimetallic selenide-filled porous carbon nanosheets for stable and highly efficient sodium-ion half/full batteries, Nanoscale 13 (44) (2021) 18578–18585, https://doi.org/10.1039/D1NR05521F.

[26] M. Dai, R. Wang, Synthesis and applications of nanostructured hollow transition metal chalcogenides, Small 17 (29) (2021) 2006813, https://doi.org/10.1002/smll.202006813.

[27] T. Jin, Q. Han, Y. Wang, L. Jiao, 1D nanomaterials: design, synthesis, and applications in sodium–ion batteries, Small 14 (2) (2018) 1703086, https://doi.org/10.1002/smll.201703086.

[28] C. Lin, G. Suo, R. Mu, B. Zhao, J. Li, X. Hou, X. Ye, Y. Yang, L. Zhang, Dual carbon confining SnO_2 nanocrystals as high-performance anode for sodium-ion batteries, J. Power Sources 623 (2024) 235426, https://doi.org/10.1016/j.jpowsour.2024.235426.

[29] J. Li, G. Suo, C. Lin, J. Li, X. Luo, G. Yang, L. Habib, Z.K. Kalkozova, K. Naseem, Synergistic electron highways and mechanical buffering in a dual-carbon confined MoS_2 anode for superior sodium-ion storage, Chem. Eng. J. 529 (2026) 173031, https://doi.org/10.1016/j.cej.2026.173031.

[30] J. Yang, C. Zhang, J. Geng, Y. Sui, H. Wei, C. Sun, H. Geng, Y. Liu, Nickel cobalt selenides on black phosphorene with fast electron transport for high-energy density sodium-ion half/full batteries, Inorg. Chem. Front. 10 (2) (2023) 424–434, https://doi.org/10.1039/D2QI01932A.

[31] W.S. Hummers Jr., R.E. Offeman, Preparation of graphitic oxide, J. Am. Chem. Soc. 80 (6) (1958) 1339, https://doi.org/10.1021/ja01539a017.

[32] J.S. Lee, J.Y. Kim, H.S. Ahn, H.S. Ka, R. Saroha, D.W. Jeong, Y.C. Kang, D.-W. Kang, J.S. Cho, Rational design strategy of multicomponent Si/$FeSeO_x$@N-Doped graphitic carbon hybrid microspheres intertwined with N-Doped carbon nanotubes as anodes for ultra-stable lithium-ion batteries, Small Struct. 6 (4) (2025) 2400354, https://doi.org/10.1002/sstr.202400354.

[33] G.T.T. Le, J. Manyam, P. Opaprakasit, N. Chanlek, N. Grisdanurak, P. Sreearunothai, Divergent mechanisms for thermal reduction of graphene oxide and their highly different ion affinities, Diam. Relat. Mater. 89 (2018) 246–256, https://doi.org/10.1016/j.diamond.2018.09.006.

[34] H. Chen, Q. Liu, S. Cao, Carbon-coated iron selenide derived from double-framework as an advance anode for Na-ion battery, J. Colloid Interface Sci. 652 (2023) 619–626, https://doi.org/10.1016/j.jcis.2023.07.126.

[35] B. Cong, S. Sun, B. Wang, C. Lv, J. Zhao, F. Jin, J. Jia, G. Chen, Iron selenide nanoparticles-encapsulated within bamboo-like N-doped carbon nanotubes as composite anodes for superior lithium and sodium-ion storage, Chem. Eng. J. 435 (2022) 135185, https://doi.org/10.1016/j.cej.2022.135185.

[36] L. Li, P. Ma, S. Hussain, L. Jia, D. Lin, X. Yin, Y. Lin, Z. Cheng, L. Wang, FeS_2/carbon hybrids on carbon cloth: a highly efficient and stable counter electrode for dye-sensitized solar cells, Sustain. Energy Fuels 3 (2019) 1749–1756, https://doi.org/10.1039/c9se00240e.

[37] P.S. Bagus, C.J. Nelin, C. Brundle, B.V. Crist, N. Lahiri, K.M. Rosso, Origin of the complex main and satellite features in Fe 2p XPS of Fe_2O_3, Phys. Chem. Chem. Phys. 24 (2022) 4562–4575, https://doi.org/10.1039/d1cp04886d.
[38] M. Cai, Z. Huang, M. Xu, S. Li, Y. Wang, H. Gu, X. Cao, Hollow $CoNiSe_4/Fe_3Se_4$ trimetallic selenides derived from zeolitic imidazolate Framework-67 as efficient electrocatalysts for oxygen evolution reaction, Langmuir 41 (35) (2025) 23558–23567, https://doi.org/10.1021/acs.langmuir.5c02671.
[39] Z. Kong, L. Wang, S. Iqbal, B. Zhang, B. Wang, J. Dou, F. Wang, Y. Qian, M. Zhang, L. Xu, Iron selenide-based heterojunction construction and defect engineering for fast Potassium/sodium-ion storage, Small 18 (15) (2022) 2107252, https://doi.org/10.1002/smll.202107252.
[40] Y. Liu, C. Yang, Y. Li, F. Zheng, Y. Li, Q. Deng, W. Zhong, G. Wang, T. Liu, $FeSe_2$/nitrogen-doped carbon as anode material for potassium-ion batteries, Chem. Eng. J. 393 (2020) 124590, https://doi.org/10.1016/j.cej.2020.124590.
[41] X. Zhang, J. Diao, J. Qiao, Y. Wen, H. Zhang, R. Wang, Confined oriented growth of $FeSe_2$ on a porous graphene film as a binder-free anode for high-rate lithium-ion batteries, Mater. Adv. 4 (2023) 4190–4196, https://doi.org/10.1039/D3MA00269A.
[42] B. Wang, K. Srinivas, X. Wang, Z. Su, B. Yu, Y. Liu, F. Ma, D. Yang, Y. Chen, Self-assembled $CoSe_2$–$FeSe_2$ heteronanoparticles along the carbon nanotube network for boosted oxygen evolution reaction, Nanoscale 13 (2021) 9651–9658, https://doi.org/10.1039/d1nr01092a.
[43] H. Fan, H. Yu, Y. Zhang, J. Guo, Z. Wang, H. Wang, N. Zhao, Y. Zheng, C. Du, Z. Dai, Q. Yan, J. Xu, 1D to 3D hierarchical iron selenide hollow nanocubes assembled from $FeSe_2$@C core-shell nanorods for advanced sodium ion batteries, Energy Storage Mater. 10 (2018) 48–55, https://doi.org/10.1016/j.ensm.2017.08.006.
[44] H.H. Do, Q.V. Le, J.H. Cho, S.H. Ahn, S.Y. Kim, Comparative study on hydrogen evolution reaction of various cobalt-selenide-based electrocatalysts, Int. J. Energy Res. 2023 (1) (2023) 6016603, https://doi.org/10.1155/2023/6016603.
[45] S.H. Yang, J.M. Choi, R. Saroha, S.W. Cho, Y.C. Kang, J.S. Cho, Hollow porous carbon nanospheres containing polar cobalt sulfide (Co_9S_8) nanocrystals as electrocatalytic interlayers for the reutilization of polysulfide in lithium–sulfur batteries, J. Colloid Interface Sci. 645 (2023) 33–44, https://doi.org/10.1016/j.jcis.2023.04.083.
[46] M. Almarzoge, M. Gencten, G. Ozsin, Exploring chlorine doping of graphene oxide synthesized via chronoamperometry for enhanced sodium-ion battery anode performance, Kor. J. Chem. Eng. 42 (2025) 3499–3514, https://doi.org/10.1007/s11814-025-00556-4.
[47] M.R.I. Rocky, V. Nulu, K.Y. Sohn, Electrochemical performance of N-Doped graphite @Carbon/red phosphorous composite for lithium-ion secondary batteries, Kor. J. Chem. Eng. 42 (2025) 1693–1704, https://doi.org/10.1007/s11814-025-00481-6.
[48] Y. Wu, Y. Huang, H. Huang, Y. Muhammad, Z. Huang, J. Winarta, Y. Zhang, S. Nie, Z. Zhao, B. Mu, Porous Fe@C composites derived from silkworm excrement for effective separation of anisole compounds, Kor. J. Chem. Eng. 4 (25) (2019) 21204–21213, https://doi.org/10.1021/acsomega.9b02681.
[49] R. Saroha, J.H. Oh, J.S. Lee, Y.C. Kang, S.M. Jeong, D.-W. Kang, C. Cho, J.S. Cho, Hierarchically porous nanofibers comprising multiple core–shell Co_3O_4@graphitic carbon nanoparticles grafted within N-doped CNTs as functional interlayers for excellent Li–S batteries, Chem. Eng. J. 426 (2021) 130805, https://doi.org/10.1016/j.cej.2021.130805.
[50] J. Kang, J. Park, M.L. Seol, I. Nam, W.S. Jung, Atomically dispersed Fe-N-S-Doped carbon as an efficient Li-S battery host for capturing polysulfides, Kor. J. Chem. Eng. 41 (2024) 1209–1216, https://doi.org/10.1007/s11814-024-00036-1.
[51] J.Y. Lee, N.Y. Kim, D.Y. Shin, H.-Y. Park, S.-S. Lee, S. Joon Kwon, D.-H. Lim, K. W. Bong, J.G. Son, J.Y. Kim, Nitrogen-doped graphene-wrapped iron nanofragments for high-performance oxygen reduction electrocatalysts, J. Nano Res. 19 (2017) 98, https://doi.org/10.1007/s11051-017-3793-y.
[52] A.C. Ferrari, D.M. Basko, Raman spectroscopy as a versatile tool for studying the properties of graphene, Nat. Nanotechnol. 8 (2013) 235–246, https://doi.org/10.1038/nnano.2013.46.
[53] Y. Feng, S. Wang, H. Wang, Y. Zhong, Y. Hu, An efficient and stable Ni–Fe selenides/nitrogen-doped carbon nanotubes in situ-derived electrocatalyst for oxygen evolution reaction, Energy Mater 55 (2020) 13927–13937, https://doi.org/10.1007/s10853-020-05002-w.
[54] S. Lee, D.W. Kang, J.H. Kwak, S. Shin, J.-W. Park, S.-H. Yu, H.-G. Jung, B.G. Kim, H.-D. Lim, Gold-incorporated porous hollow carbon nanofiber for reversible magnesium-metal batteries, Chem. Eng. J. 431 (2022) 133968, https://doi.org/10.1016/j.cej.2021.133968.
[55] T. Zeng, D. Feng, Q. Liu, R. Zhou, Confining Nano-GeP in nitrogenous hollow carbon fibers toward flexible and high-performance lithium-ion batteries, ACS Appl. Mater. Interfaces 13 (2021) 32978–32988, https://doi.org/10.1021/acsami.1c07387.
[56] H. Peng, Z. Mo, S. Liao, H. Liang, L. Yang, F. Luo, H. Song, Y. Zhong, B. Zhang, High performance Fe- and N-doped carbon catalyst with graphene structure for oxygen reduction, Sci. Rep. 3 (2013) 1765, https://doi.org/10.1038/srep01765.
[57] S. Zhou, R. Jiang, S. Wang, L. Yu, X. Shi, L. Shao, Z. Sun, L. Hang, $FeSe_2$ micro-nanorods confined in N-doped carbon as an advanced anode for fast sodium ion storage, J. Mater. Chem. A 12 (2024) 11028–11037, https://doi.org/10.1039/d4ta00097h.
[58] J. Zhang, Y. Liu, H. Liu, Y. Song, S. Sun, Q. Li, X. Xing, J. Chen, Urchin-like Fe_3Se_4 hierarchitectures: a novel pseudocapacitive sodium-ion storage anode with prominent rate and cycling properties, Small 16 (26) (2020) 2000504, https://doi.org/10.1002/smll.202000504.
[59] J.H. Choi, S.-K. Park, Y.C. Kang, A salt-templated strategy toward hollow iron selenides graphitic carbon composite microspheres with interconnected multicavities as high-performance anode materials for sodium-ion batteries, Small 15 (2) (2019) 1803043, https://doi.org/10.1002/smll.201803043.
[60] Q. Shi, S. Liu, X. Liu, J. Guo, Z. Qin, J. Tong, Mo-doped and vacancy-rich Ni_2P@NC anode: a dual-strategy approach to high-capacity and long cycle life sodium-ion batteries, J. Colloid Interface Sci. 701 (2026) 138711, https://doi.org/10.1016/j.jcis.2025.138711.
[61] J.C. Xi, Y.F. Yuan, M. Zhu, S.M. Yin, Y.B. Chen, S.Y. Guo, P.F. Du, Achieving long-life and efficient sodium storage through encapsulating Fe_3Se_4 nanoparticles within hollow mesoporous carbon nanospheres, J. Energy Storage 81 (2024) 110499, https://doi.org/10.1016/j.est.2024.110499.
[62] H. Ma, D. Li, Z. Zhang, C. Wang, J. Zheng, L. Guo, Suppressing sodium trapping and structural collapse in $FeSe_2$ anodes *via* high-graphitic-N-doped carbon confinement for long-cycling sodium-ion batteries, J. Energy Storage 142 (2026) 119590, https://doi.org/10.1016/j.est.2025.119590.
[63] D. Li, J. Zhou, X. Chen, H. Song, Achieving ultrafast and stable Na-Ion storage in $FeSe_2$ nanorods/graphene anodes by controlling the surface oxide, ACS Appl. Mater. Interfaces 10 (2018) 22841–22850, https://doi.org/10.1021/acsami.8b06318.
[64] W. Zhao, X. Ma, L. Yue, L. Zhang, Y. Luo, Y. Ren, X.-E. Zhao, N. Li, B. Tang, Q. Liu, Y. Liu, S. Gao, A.A. Alshehrig, X. Sun, A gradient hexagonal-prism Fe_3Se_4@SiO_2@C configuration as a highly reversible sodium conversion anode, J. Mater. Chem. A 10 (2022) 4087–4099, https://doi.org/10.1039/D1TA10571J.
[65] Z. Cheng, T. Du, L. Zhou, H. Wang, L. Cao, Engineering nano-size carbon-coated Fe_3O_4 anode for long cycle life and accelerated reaction kinetics in lithium/sodium ion batteries, J. Colloid Interface Sci. 700 (2025) 138347, https://doi.org/10.1016/j.jcis.2025.138347.
[66] H.S. Ka, G.H. Oh, J.H. Baek, J.S. Lee, J.-S. Park, J.S. Cho, Rational design of porous SnO_2/Fe_xO_y composite microspheres with polydopamine-derived N-doped carbon coating layer as high-performance anode for lithium-ion batteries, J. Ind. Eng. Chem. 156 (2025) 588–600, https://doi.org/10.1016/j.jiec.2025.09.004.